

# Bayesian Pose Graph Optimization via Bingham Distributions and Tempered Geodesic MCMC

Tolga Birdal\*    Umut Şimşekli†    M. Onur Eken‡    Slobodan Ilic§

October 7, 2021

## Abstract

We introduce Tempered Geodesic Markov Chain Monte Carlo (TG-MCMC) algorithm for initializing pose graph optimization problems, arising in various scenarios such as SFM (structure from motion) or SLAM (simultaneous localization and mapping). TG-MCMC is first of its kind as it unites asymptotically global non-convex optimization on the spherical manifold of quaternions with posterior sampling, in order to provide both reliable initial poses and uncertainty estimates that are informative about the quality of individual solutions. We devise rigorous theoretical convergence guarantees for our method and extensively evaluate it on synthetic and real benchmark datasets. Besides its elegance in formulation and theory, we show that our method is robust to missing data, noise and the estimated uncertainties capture intuitive properties of the data.

## Contents

<b>1</b>	<b>Introduction</b>	<b>1</b>
<b>2</b>	<b>Preliminaries and Technical Background</b>	<b>2</b>
2.1	Notation and definitions . . . . .	2
2.2	Quaternions . . . . .	3
2.2.1	Manifold of quaternions . . . . .	3
2.3	The Bingham Distribution . . . . .	3
<b>3</b>	<b>The Proposed Model</b>	<b>4</b>
<b>4</b>	<b>Tempered Geodesic Monte Carlo for Pose Graph Optimization</b>	<b>5</b>
4.1	Connection between sampling and optimization . . . . .	5
4.2	Construction of the algorithm . . . . .	6
4.3	Numerical integration . . . . .	6
4.4	Theoretical analysis . . . . .	7

\*Technical University of Munich and Siemens AG. Email: [tolga.birdal@tum.de](mailto:tolga.birdal@tum.de).

†LTCI, Télécom Paristech, Université Paris-Saclay. Email: [umut.simsekli@telecom-paristech.fr](mailto:umut.simsekli@telecom-paristech.fr).

‡Technical University of Munich. Email: [onur.eken@tum.de](mailto:onur.eken@tum.de).

§Siemens AG. Email: [slobodan.ilic@siemens.com](mailto:slobodan.ilic@siemens.com).

<b>5 Experiments</b>	<b>8</b>
5.1 Synthetic Evaluations . . . . .	8
5.1.1 Robustness to Noise . . . . .	9
5.1.2 Outlier Resilience . . . . .	9
5.1.3 Projected Gradient Descent . . . . .	10
5.2 Results in Real Data . . . . .	10
5.2.1 Uncertainty Estimation in Real Data . . . . .	12
5.2.2 Graph Evolution . . . . .	12
<b>6 Conclusion</b>	<b>12</b>
<b>References</b>	<b>12</b>
<b>Appendix</b>	<b>17</b>
<b>A Comparison to exponential coordinates</b>	<b>17</b>
<b>B Numerical Integration</b>	<b>18</b>
B.1 Update equations for the rotation components . . . . .	18
B.2 Update equations for the translation components . . . . .	18
B.3 Algorithm pseudocode . . . . .	19
<b>C Assumptions</b>	<b>19</b>
<b>D Proof of Proposition 1</b>	<b>20</b>
<b>E Proof of Theorem 1</b>	<b>20</b>
<b>F Proof of Corollary 1</b>	<b>20</b>
<b>G Proof of Lemma 1</b>	<b>21</b>
<b>H Technical Results</b>	<b>23</b>
<b>I Gradients of Likelihood and Prior Terms</b>	<b>25</b>
<b>J Used Datasets</b>	<b>27</b>

# 1 Introduction

The ability to navigate autonomously is now a key technology in self driving cars, unmanned aerial vehicles (UAV), robot guidance, augmented reality, 3D digitization, sensory network localization and more. This ubiquitous appliance is due to the fact that vision sensors can provide cues to directly solve 6DoF pose estimation problem and does not necessitate external tracking input, such as imprecise GPS, to ego-localize. Many of the problems in these domains can now be addressed by tailor-made pipelines such as SLAM (Simultaneous Localization and Mapping), SfM (Structure From Motion) or multi robot localization (MRL) [KPZK17, CC18]. Nowadays, thanks to the resulting reliable estimates of rotations and translations, many of these pipelines rely on some form of an optimization, such as bundle adjustment (BA) [TMHF99] or 3D global registration [BI17, HH03], that can globally consider the acquired measurements. Holistically, these methods belong to the family of *pose graph optimization* (PGO) [KGS<sup>+</sup>11]. Unfortunately, many of PGO post-processing stages, which take in to account both camera poses and 3D structure, are too costly for online or even soft-realtime operation. This bottleneck demands good solutions for PGO initialization, that can relieve the burden of the joint optimization.

In this paper, we address the particular problem of initializing PGO, in which multiple local measurements are fused into a globally consistent estimate, without resorting to the costly bundle adjustment or optimization that uses structure. In specifics, let us consider a finite simple directed graph  $G = (V, E)$ , where vertices correspond to reference frames and edges to the available relative measurements as shown in Figures 1(a), 1(b). Both vertices and edges are labeled with rigid motions representing absolute and relative poses, respectively. Each absolute pose is described by a homogeneous transformation matrix  $\{\mathbf{M}_i \in SE(3)\}_{i=1}^n$ . Similarly, each relative pose is expressed as the transformation between frames  $i$  and  $j$ ,  $\mathbf{M}_{ij}$ , where  $(i, j) \in E \subset [n] \times [n]$ . The labeling of the edges is such that if  $(i, j) \in E$ , then  $(j, i) \in E$  and  $\mathbf{M}_{ij} = \mathbf{M}_{ji}^{-1}$ . Hence, we consider  $G$  to be undirected. With a convention as shown in Figure 1(c), the link between absolute and relative transformations is encoded by the *compatibility constraint*:

$$\mathbf{M}_{ij} \approx \mathbf{M}_j \mathbf{M}_i^{-1}, \forall i \neq j \quad (1)$$

Primarily motivated by Govindu et. al. [Gov01], *rigid-motion synchronization* initializes PGO by computing an estimate of the vertex labels  $\mathbf{M}_i$  (absolute poses) given enough measurements of the ratios  $\mathbf{M}_{ij}$ . In other words, it tries to find the absolute poses that best fit the relative pairwise measurements. Typically, in order to remove the gauge freedom, one of the poses is set to identity  $\mathbf{M}_0 = \mathbf{I}$  and the problem reduces to recovering  $n - 1$  absolute poses. The solution is the state of the art method to initialize, say SfM [KPZK17, CTDD15, TZD16] thanks to the good quality of the estimates.

The pose graph optimization problem is often formed as non-convex optimization problems, opening up room for different formulations and approaches. Direct methods try to compute a good initial solution [FO12, CTDD15, AFR15, AFR16], which are then refined by iterative techniques [TRA11, Gov04]. Robustness to outlier relative pose estimates is also crucial for a better solution [CG13, HAT11, TZD16, CG18, CC18]. The structure of our peculiar problem allows for global optimization, when isotropic noise is assumed and under reasonable noise levels as well as well connected graph structures [FO12, WBS16, RCBL16, BGJ16, EOFC18, BGJ17]. It is also noteworthy that, even though the problem has been previously handled with statistical approaches [TD14], up until now, to the best of our knowledge, estimation of uncertainties in PGO initialization are never truly considered.

In this paper, we look at the graph optimization problem from a probabilistic point of view. We begin by representing the problem on the Cartesian product of the true Riemannian manifold of quaternions and Euclidean manifold of translations. We model rotations with Bingham distributions [Bin74] and translation with Gaussians. The probabilistic framework provides two important features: (i) we can align the modes of the data (relative motions) with the posterior parameters, (ii) we can quantify

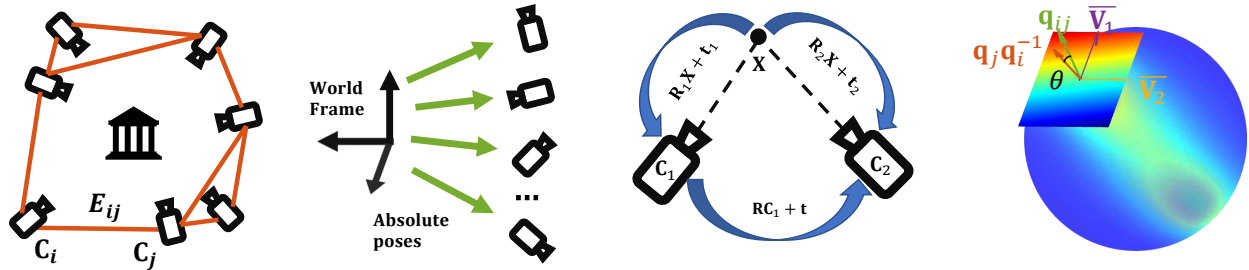


Figure 1: From left to right: (a) Initial pose graph of relative poses. (b) Absolute poses w.r.t. common frame. (c) Convention used to describe the pairwise relationships. (d) A sample Bingham distribution and the rotational components.

the uncertainty of our estimates by using the posterior predictive distributions. In order to achieve these goals, we come up with efficient algorithms both for maximum a-posteriori (MAP) estimation and posterior sampling: ‘tempered’ geodesic Markov Chain Monte Carlo (TG-MCMC). Controlled by a single parameter, TG-MCMC can either work as a standard MCMC algorithm that can generate samples from a Bayesian posterior, whose entropy, or covariance, as well as the samples themselves, provide necessary cues for uncertainty estimation - both on camera poses and possibly on the 3D structure, or it can work as an optimization algorithm that is able to generate samples around *the global optimum* of the MAP estimation problem. In this perspective, TG-MCMC bridges the gap between Bayesian geodesic Markov Chain Monte Carlo (gMCMC) and non-convex optimization, as we will theoretically present.

In a nutshell, our contributions are as follows:

- Novel probabilistic model using Bingham distributions in pose averaging for the first time,
- Tempered gMCMC: Novel tempered MCMC algorithm for global optimization and sampling on the manifolds using the known geodesic flow,
- Theoretical understanding and convergence guarantees for the devised algorithm,
- Strong experimental results justifying the validity of the approach.

## 2 Preliminaries and Technical Background

### 2.1 Notation and definitions

$x \in \mathbb{R}$  is a scalar. We denote vectors by lower case bold letters  $\mathbf{x} = (x_1 \cdots x_N) \in \mathbb{R}^N$ . A square matrix  $\mathbf{X} = (X_{ij}) \in \mathbb{R}^{N \times N}$ .  $\mathbf{I}_{N \times N}$  is the identity matrix. Rotations belong to the special orthogonal group  $\mathbf{R} \in SO(3)$ . With translations  $\mathbf{t} \in \mathbb{R}^3$ , they form the 3D special Euclidean group  $SE(3)$ . We also define an  $m$ -dimensional *Riemannian manifold*  $\mathcal{M}$ , endowed with a *Riemannian metric*  $\mathbf{G}$  to be a smooth curved space, equipped with the inner product  $\langle \mathbf{u}, \mathbf{v} \rangle_x = \mathbf{u}^T \mathbf{G} \mathbf{v}$  in the tangent space  $\mathcal{T}_x \mathcal{M}$ , embedded in an ambient higher-dimensional Euclidean space  $\mathbb{R}^n$ . One such manifold is the unit hypersphere in  $\mathbb{R}^d$ :  $\mathbb{S}^{d-1} = \{\mathbf{x} \in \mathbb{R}^d : \|\mathbf{x}\| = 1\} \subset \mathbb{R}^d$ . A vector  $\mathbf{v}$  is said to be *tangent* to a point  $\mathbf{x} \in \mathcal{M}$  if  $\mathbf{x}^T \mathbf{v} = 0$ . A tangent space is the set  $\mathcal{T}_x$  of all such vectors:  $\mathcal{T}_x = \{\mathbf{v} \in \mathbb{R}^d : \mathbf{x}^T \mathbf{v} = 0\}$ . We define the geodesic on the manifold to be a constant speed, length minimizing curve between  $\mathbf{x}, \mathbf{y} \in \mathcal{M}$ ,  $\gamma : [0, 1] \rightarrow \mathcal{M}$ , with  $\gamma(0) = \mathbf{x}$  and  $\gamma(1) = \mathbf{y}$ .

## 2.2 Quaternions

A *quaternion*  $\mathbf{q}$  is an element of Hamilton algebra  $\mathbb{H}$ , extending the complex numbers with three imaginary units  $\mathbf{i}, \mathbf{j}, \mathbf{k}$  in the form  $\mathbf{q} = q_1\mathbf{1} + q_2\mathbf{i} + q_3\mathbf{j} + q_4\mathbf{k} = (q_1, q_2, q_3, q_4)^T$ , with  $(q_1, q_2, q_3, q_4)^T \in \mathbb{R}^4$  and  $\mathbf{i}^2 = \mathbf{j}^2 = \mathbf{k}^2 = \mathbf{ijk} = -\mathbf{1}$ . We also write  $\mathbf{q} := [a, \mathbf{v}]$  with the scalar part  $a = q_1 \in \mathbb{R}$  and the vector part  $\mathbf{v} = (q_2, q_3, q_4)^T \in \mathbb{R}^3$ . The conjugate  $\bar{\mathbf{q}}$  of the quaternion  $\mathbf{q}$  is given by  $\bar{\mathbf{q}} := q_1 - q_2\mathbf{i} - q_3\mathbf{j} - q_4\mathbf{k}$ . A versor or *unit quaternion*  $\mathbf{q} \in \mathbb{H}_1$  with  $1 \stackrel{!}{=} \|\mathbf{q}\| := \mathbf{q} \cdot \bar{\mathbf{q}}$  and  $\mathbf{q}^{-1} = \bar{\mathbf{q}}$ , gives a compact and numerically stable parametrization to represent orientation of objects in  $\mathbb{S}^3$ , avoiding gimbal lock and singularities [LF<sup>+</sup>05]. Identifying antipodal points  $\mathbf{q}$  and  $-\mathbf{q}$  with the same element, the unit quaternions form a double covering group of  $SO(3)$ . The non-commutative multiplication of two quaternions  $\mathbf{p} := [p_1, \mathbf{v}_p]$  and  $\mathbf{r} := [r_1, \mathbf{v}_r]$  is defined to be  $\mathbf{p} \otimes \mathbf{r} = [p_1r_1 - \mathbf{v}_p \cdot \mathbf{v}_r, p_1\mathbf{v}_r + r_1\mathbf{v}_p + \mathbf{v}_p \times \mathbf{v}_r]$ . For simplicity we use  $\mathbf{p} \otimes \mathbf{r} := \mathbf{p} \cdot \mathbf{r} := \mathbf{pr}$ .

### 2.2.1 Manifold of quaternions

Unit quaternions form a hyperspherical manifold,  $\mathbb{S}^3$ , that is an embedded Riemannian submanifold of  $\mathbb{R}^4$ . This forms a Hausdorff space, where each point has an open neighborhood homeomorphic to the open N-dimensional disc, called an N-manifold. Due to the topology of the sphere, there is no unique way find a globally covering coordinate patch. It is hence common to use local exponential and logarithmic maps that can be sphere-specifically defined as:  $\text{Exp}(\mathbf{x}, \mathbf{v}) = \mathbf{x} \cos(\theta) + \mathbf{v} \sin(\theta)/\theta$ , where  $\mathbf{v}$  denotes a tangent vector to  $\mathbf{x}$ . This property decorates quaternions with a known analytic geodesic flow, given by [BG13]:

$$[\mathbf{x}(t) \quad \mathbf{v}(t)] = [\mathbf{x}(0) \quad \mathbf{v}(0)] \begin{bmatrix} 1 & 0 \\ 0 & 1/\alpha \end{bmatrix} \begin{bmatrix} \cos(\alpha t) & -\sin(\alpha t) \\ \sin(\alpha t) & \cos(\alpha t) \end{bmatrix} \begin{bmatrix} 1 & 0 \\ 0 & \alpha \end{bmatrix} \quad (2)$$

where  $\alpha \triangleq \|\mathbf{v}(0)\|$ . It is also useful to think about a quaternion as the normal vector to itself, due to the unitness of the hypersphere. By this property, projection onto  $\mathcal{T}_x$  reads  $P(\mathbf{x}) = \mathbf{I} - \mathbf{x}\mathbf{x}^T$  [BG13].

## 2.3 The Bingham Distribution

Derived from a zero-mean Gaussian, the Bingham distribution [Bin74] is an antipodally symmetric probability distribution conditioned to lie on  $\mathbb{S}^{d-1}$  with probability density function (PDF)  $\mathcal{B} : \mathbb{S}^{d-1} \rightarrow R$ :

$$\mathcal{B}(\mathbf{x}; \mathbf{\Lambda}, \mathbf{V}) = (1/F) \exp(\mathbf{x}^T \mathbf{V} \mathbf{\Lambda} \mathbf{V}^T \mathbf{x}) = (1/F) \exp\left(\sum_{i=1}^d \lambda_i (\mathbf{v}_i^T \mathbf{x})^2\right) \quad (3)$$

where  $\mathbf{V} \in \mathbb{R}^{d \times d}$  is an orthogonal matrix ( $\mathbf{V}\mathbf{V}^T = \mathbf{V}^T\mathbf{V} = \mathbf{I}_{d \times d}$ ) describing the orientation,  $\mathbf{\Lambda} = \text{diag}(0, \lambda_1, \dots, \lambda_{d-1}) \in \mathbb{R}^{d \times d}$  with  $0 \geq \lambda_1 \geq \dots \geq \lambda_{d-1}$  is the concentration matrix, and  $F$  is a normalization constant. With this formulation, the mode of the distribution is obtained as the first column of  $\mathbf{V}$ . The antipodal symmetry of the PDF makes it amenable to explain the topology of quaternions, i. e.,  $\mathcal{B}(\mathbf{x}; \cdot) = \mathcal{B}(-\mathbf{x}; \cdot)$  holds for all  $\mathbf{x} \in \mathbb{S}^{d-1}$ . When  $d = 4$  and  $\lambda_1 = \lambda_2 = \lambda_3$ , it is safe to write  $\mathbf{\Lambda} = \text{diag}([1, 0, 0, 0])$ . In this case, the logarithm of the Bingham density reduces to the dot product of two quaternions  $\mathbf{q}_1 \triangleq \mathbf{x}$  and the mode of the distribution, say  $\bar{\mathbf{q}}_2$ . For rotations, this induces a metric,  $d_{\text{bingham}} = (\mathbf{q}_1 \cdot \bar{\mathbf{q}}_2)^2 = \cos(\theta/2)^2$ , that is closely related to the true Riemannian distance  $d_{\text{riemann}} = \|\log(\mathbf{R}_1 \mathbf{R}_2^T)\| \triangleq 2\arccos(|\mathbf{q}_1 \bar{\mathbf{q}}_2|) \triangleq 2\arccos(\sqrt{d_{\text{bingham}}})$ . Bingham distributions have been extensively used to represent distributions on quaternions [GBR12, KGJH13, GK14]; however, to the best of our knowledge, never for the problem at hand.

### 3 The Proposed Model

In this section, we will describe our proposed model for PGO initialization. We consider the situation where we observe a set of noisy pairwise pose estimations  $\mathbf{M}_{ij}$ , represented by *augmented quaternions* as  $\{\mathbf{q}_{ij} \in \mathbb{S}^3 \subset \mathbb{R}^4, \mathbf{t}_{ij} \in \mathbb{R}^3\}$ . The indices  $(i, j) \in E$  run over the edges the graph. We assume that the observations  $\{\mathbf{q}_{ij}, \mathbf{t}_{ij}\}_{(i,j) \in E}$  are generated by a probabilistic model that has the following hierarchical structure:

$$\mathbf{q}_i \sim p(\mathbf{q}_i), \quad \mathbf{t}_i \sim p(\mathbf{t}_i), \quad \mathbf{q}_{ij}|\cdot \sim p(\mathbf{q}_{ij}|\mathbf{q}_i, \mathbf{q}_j), \quad \mathbf{t}_{ij}|\cdot \sim p(\mathbf{t}_{ij}|\mathbf{q}_i, \mathbf{q}_j, \mathbf{t}_i, \mathbf{t}_j), \quad (4)$$

where the *latent variables*  $\{\mathbf{q}_i \in \mathbb{S}^3\}_{i=1}^n$  and  $\{\mathbf{t}_i \in \mathbb{R}^3\}_{i=1}^n$  denote the true values of the *absolute poses* and *absolute translations* with respect to a common origin, corresponding to  $\mathbf{M}_i$  of Eq. 1. Here,  $p(\mathbf{q}_i)$  and  $p(\mathbf{t}_i)$  denote the *prior distributions* of the latent variables, and the product of the densities  $p(\mathbf{q}_{ij}|\cdot)$  and  $p(\mathbf{t}_{ij}|\cdot)$  forms the *likelihood function*.

By respecting the natural manifolds of the latent variables, we choose the following prior model:  $\mathbf{q}_i \sim \mathcal{B}(\mathbf{\Lambda}_p, \mathbf{V}_p)$ ,  $\mathbf{t}_i \sim \mathcal{N}(\mathbf{0}, \sigma_p^2 \mathbf{I})$  where  $\mathbf{\Lambda}_p$ ,  $\mathbf{V}_p$ , and  $\sigma_p^2$  are the prior model parameters, which are assumed to be known. We then choose the following model for the observed variables:

$$\mathbf{q}_{ij}|\mathbf{q}_i, \mathbf{q}_j \sim \mathcal{B}(\mathbf{\Lambda}, \mathbf{V}(\mathbf{q}_j \bar{\mathbf{q}}_i)), \quad \mathbf{t}_{ij}|\mathbf{q}_i, \mathbf{q}_j, \mathbf{t}_i, \mathbf{t}_j \sim \mathcal{N}(\boldsymbol{\mu}_{ij}, \sigma^2 \mathbf{I}), \quad (5)$$

where  $\mathbf{\Lambda}$  is a fixed,  $\mathbf{V}$  is a matrix-valued function that will be defined in the sequel;  $\boldsymbol{\mu}_{ij}$  denotes the expected value of  $\mathbf{t}_{ij}$  provided that the values of the relevant latent variables  $\mathbf{q}_i, \mathbf{q}_j, \mathbf{t}_i, \mathbf{t}_j$  are known, and has the form:  $\boldsymbol{\mu}_{ij} \triangleq \mathbf{t}_j - (\mathbf{q}_j \bar{\mathbf{q}}_i) \mathbf{t}_i (\mathbf{q}_i \bar{\mathbf{q}}_j)$ . With this modeling strategy, we are expecting that  $\mathbf{t}_{ij}$  would be close to the true translation  $\boldsymbol{\mu}_{ij}$  that is a deterministic function of the absolute poses. Our strategy also lets  $\mathbf{t}_{ij}$  differ from  $\boldsymbol{\mu}_{ij}$  and the level of this flexibility is determined by  $\sigma^2$ .

Constructing Bingham distribution on any given mode  $\mathbf{q} \in \mathbb{S}^3$  requires finding a frame bundle  $\mathbb{S}^3 \rightarrow \mathcal{F}\mathbb{S}^3$  composed of the unit vector (the mode) and its orthonormals. Being *parallelizable* ( $d = 1, 2, 4$  or  $8$ ), manifold of unit quaternions enjoys an injective homomorphism to the orthonormal matrix ring composed of the orthonormal basis [Ste51]. Thus, we define  $\mathbf{V} : \mathbb{S}^3 \mapsto \mathbb{R}^{4 \times 4}$  as follows:

$$\mathbf{V}(\mathbf{q}) \triangleq \begin{bmatrix} q_1 & -q_2 & -q_3 & q_4 \\ q_2 & q_1 & q_4 & q_3 \\ q_3 & -q_4 & q_1 & -q_2 \\ q_4 & q_3 & -q_2 & -q_1 \end{bmatrix}. \quad (6)$$

It is easy to verify that  $\mathbf{V}(\mathbf{q})$  is orthonormal for every  $\mathbf{q} \in \mathbb{S}^3$ .  $\mathbf{V}(\mathbf{q})$  further gives a convenient notation for representing quaternions as matrices paving the way to linear operations, such as quaternion multiplication or orthonormalization without pesky Gram-Schmidt processes. By using the definition of  $\mathbf{V}(\mathbf{q})$  and assuming that the diagonal entries of  $\mathbf{\Lambda}$  are sorted in decreasing order, we have the following property:

$$\arg \max_{\mathbf{q}_{ij}} \{p(\mathbf{q}_{ij}|\mathbf{q}_i, \mathbf{q}_j) = \mathcal{B}(\mathbf{\Lambda}, \mathbf{V}(\mathbf{q}_j \bar{\mathbf{q}}_i))\} = \mathbf{q}_j \bar{\mathbf{q}}_i. \quad (7)$$

Similar to the proposed observation model for the relative translations, given the true poses  $\mathbf{q}_i, \mathbf{q}_j$ , this modeling strategy sets the most likely value of the relative pose to the deterministic value  $\mathbf{q}_j \bar{\mathbf{q}}_i$ , and also lets  $\mathbf{q}_{ij}$  differ from this value up to the extent determined by  $\mathbf{\Lambda}$ . This configuration is illustrated in Fig 1(d).

Representing  $SE(3)$  in the form of a quaternion-translation parameterization, we can now formulate the motion-synchronization problem as a probabilistic inference problem. In particular we are interested in the following two quantities:

1. The maximum a-posteriori (MAP) estimate:  $(\mathbf{Q}^*, \mathbf{T}^*) = \arg \max_{\mathbf{Q}, \mathbf{T}} p(\mathbf{Q}, \mathbf{T} | \mathcal{D}) =$

$$\arg \max_{\mathbf{Q}, \mathbf{T}} \left( \sum_{(i,j) \in E} \{ \log p(\mathbf{q}_{ij} | \mathbf{Q}, \mathbf{T}) + \log p(\mathbf{t}_{ij} | \mathbf{Q}, \mathbf{T}) \} + \sum_i \log p(\mathbf{q}_i) + \sum_i \log p(\mathbf{t}_i) \right), \quad (8)$$

where  $\mathcal{D} \equiv \{\mathbf{q}_{ij}, \mathbf{t}_{ij}\}_{(i,j) \in E}$  denotes the observations,  $\mathbf{Q} \equiv \{\mathbf{q}_i\}_{i=1}^n$  and  $\mathbf{T} \equiv \{\mathbf{t}_i\}_{i=1}^n$ .

2. The full posterior distribution:  $p(\mathbf{Q}, \mathbf{T} | \mathcal{D}) \propto p(\mathcal{D} | \mathbf{Q}, \mathbf{T}) \times p(\mathbf{Q}) \times p(\mathbf{T})$ .

Both of these problems are very challenging and cannot be directly addressed by standard methods such as gradient descent (problem 1) or standard MCMC methods (problem 2). The difficulty in these problems is mainly originated by the fact that the posterior density is non-log-concave (i.e. the negative log-posterior is non-convex) and any algorithm that aims at solving one of these problems should be able to operate in the particular manifold of this problem, that is  $(\mathbb{S}^3)^n \times \mathbb{R}^{3n} \subset \mathbb{R}^{7n}$ .

## 4 Tempered Geodesic Monte Carlo for Pose Graph Optimization

### 4.1 Connection between sampling and optimization

In a recent study [LZS16], Liu et al. proposed the stochastic gradient geodesic Monte Carlo (SG-GMC) as an extension to [BG13] and provided a practical posterior sampling algorithm for the problems that are defined on manifolds whose geodesic flows are analytically available. Since our augmented quaternions form such a manifold<sup>1</sup>, we can use this algorithm for generating (approximate) samples from the posterior distribution, which would address the second problem defined in Section 3.

Recent studies have shown that stochastic-gradient MCMC (SG-MCMC) techniques are closely related to optimization and they indeed have a strong potential in non-convex problems due to their randomized nature. In particular, it has been recently shown that, a simple variant of SG-MCMC is guaranteed to converge to a point near a local optimum in polynomial time [ZLC17, TLR18] and eventually converge to a point near the global optimum [RRT17], even in non-convex settings. Even though these recent results illustrated the advantages of SG-MCMC in optimization, it is not clear how to develop an SG-MCMC-based optimization algorithm that can operate on manifolds. In this section, we will extend the SG-GMC algorithm in this vein to obtain a *parametric* algorithm, which is able to both sample from the posterior distribution and perform optimization for obtaining the MAP estimates depending on the choice of the practitioner. In other words, the algorithm should be able to address both problems that we defined in Section 3 with theoretical guarantees.

We start by defining a more compact notation that will facilitate the presentation of the algorithm. We define the variable  $\mathbf{x} \in \mathcal{X}$ , such that  $\mathbf{x} \triangleq [\mathbf{q}_1^\top, \dots, \mathbf{q}_n^\top, \mathbf{t}_1^\top, \dots, \mathbf{t}_n^\top]^\top$  and  $\mathcal{X} \triangleq (\mathbb{S}^3)^n \times \mathbb{R}^{3n}$ . The posterior density of interest then has the form  $\pi_{\mathcal{H}}(\mathbf{x}) \triangleq p(\mathbf{x} | \mathcal{D}) \propto \exp(-U(\mathbf{x}))$  with respect to the Hausdorff measure, where  $U$  is called the *potential* energy. We define a *smooth embedding*  $\xi : \mathbb{R}^{6n} \mapsto \mathcal{X}$  such that  $\xi(\tilde{\mathbf{x}}) = \mathbf{x}$ . If we consider the embedded posterior density  $\pi_{\lambda}(\tilde{\mathbf{x}}) \triangleq p(\tilde{\mathbf{x}} | \mathcal{D})$  with respect to the Lebesgue measure, then by the area formula (cf. Theorem 1 in [DHS<sup>+</sup>13]), we have the following key property:  $\pi_{\mathcal{H}}(\mathbf{x}) = \pi_{\lambda}(\tilde{\mathbf{x}}) / \sqrt{|\mathbf{G}(\tilde{\mathbf{x}})|}$ , where  $|\mathbf{G}|$  denotes the determinant of the Riemann metric tensor  $[\mathbf{G}(\tilde{\mathbf{x}})]_{i,j} \triangleq \sum_{l=1}^{7n} \frac{\partial x_l}{\partial \tilde{x}_i} \frac{\partial x_l}{\partial \tilde{x}_j}$  for all  $i, j \in \{1, \dots, 6n\}$ .

The main idea in our approach is to introduce an *inverse temperature* variable  $\beta \in \mathbb{R}_+$  and consider the *tempered* posterior distributions whose density is proportional to  $\exp(-\beta U(\mathbf{x}))$ . When  $\beta = 1$ ,

<sup>1</sup>The manifold  $(\mathbb{S}^3)^n \times \mathbb{R}^{3n}$  can be expressed as a product of the manifolds  $\mathbb{S}^3$  ( $n$  times) and  $\mathbb{R}^{3n}$ . Therefore, its geodesic flow is the combination of the geodesic flows of individual manifolds. Since the geodesic flows in  $\mathbb{S}^{d-1}$  and  $\mathbb{R}^d$  are analytically available, so is the flow of the product manifold [BG13].

this density coincides with the original posterior; however, as  $\beta$  goes to infinity, the tempered density concentrates near the global minimum of the potential  $U$  [Hwa80, GM91]. This important property implies that, for large enough  $\beta$ , a random sample that is drawn from the tempered posterior would be close to the global optimum and can therefore be used as a MAP estimate.

## 4.2 Construction of the algorithm

We will now construct the proposed algorithm. In particular, we will first extend the continuous-time Markov process proposed in [LZS16] and develop a process whose marginal stationary distribution has a density proportional to  $\exp(-\beta U(\mathbf{x}))$  for any given  $\beta > 0$ . Then we will develop practical algorithms for generating samples from this tempered posterior.

We propose the following stochastic differential equation (SDE) in the Euclidean space by making use of the embedding  $\xi$ :

$$\begin{aligned} d\tilde{\mathbf{x}}_t &= \mathbf{G}(\tilde{\mathbf{x}}_t)^{-1} \mathbf{p}_t dt \\ d\mathbf{p}_t &= -\left( \nabla_{\tilde{\mathbf{x}}} U_\lambda(\tilde{\mathbf{x}}_t) + \frac{1}{2} \nabla_{\tilde{\mathbf{x}}} \log |\mathbf{G}| + c\mathbf{p}_t + \frac{1}{2} \nabla_{\tilde{\mathbf{x}}} (\mathbf{p}_t^\top \mathbf{G}^{-1} \mathbf{p}_t) \right) dt + \sqrt{(2c/\beta) \mathbf{M}^\top \mathbf{M}} dW_t, \end{aligned} \quad (9)$$

where  $\nabla_{\tilde{\mathbf{x}}} U_\lambda \triangleq -\nabla_{\tilde{\mathbf{x}}} \log \pi_\lambda$ ,  $\mathbf{G}$  and  $\mathbf{M}$  are short-hand notations for  $\mathbf{G}(\tilde{\mathbf{x}}_t)$  and  $[\mathbf{M}(\tilde{\mathbf{x}}_t)]_{ij} \triangleq \partial \mathbf{x}_i / \partial \tilde{\mathbf{x}}_j$ , respectively,  $\mathbf{p}_t \in \mathbb{R}^{6n}$  is called the *momentum* variable,  $c > 0$  is called the *friction*, and  $W_t$  denotes the standard Brownian motion in  $\mathbb{R}^{6n}$ .

We will first analyze the invariant measure of the SDE (9).

**Proposition 1.** *Let  $\varphi_t = [\tilde{\mathbf{x}}_t^\top, \mathbf{p}_t^\top]^\top \in \mathbb{R}^{12n}$  and  $(\varphi_t)_{t \geq 0}$  be a Markov process that is a solution of the SDE (9). Then  $(\varphi_t)_{t \geq 0}$  has an invariant measure  $\mu_\varphi$ , whose density with respect to the Lebesgue measure is proportional to  $\exp(-\mathcal{E}_\lambda(\varphi))$ , where  $\mathcal{E}_\lambda$  is defined as follows:*

$$\mathcal{E}_\lambda(\varphi) \triangleq \beta U_\lambda(\tilde{\mathbf{x}}) + \frac{\beta}{2} \log |\mathbf{G}(\tilde{\mathbf{x}})| + \frac{\beta}{2} \mathbf{p}^\top \mathbf{G}(\tilde{\mathbf{x}})^{-1} \mathbf{p}. \quad (10)$$

All the proofs are given in the appendix. By using the area formula and the definitions of  $\mathbf{G}$  and  $\mathbf{M}$ , one can show that the density of  $\mu_\varphi$  can also be written with respect to the Hausdorff measure, as follows: (see Section 3.2 in [BG13] for details)  $\mathcal{E}_\mathcal{H}(\mathbf{x}, \mathbf{v}) \triangleq \beta U_\mathcal{H} + \frac{\beta}{2} \mathbf{v}^\top \mathbf{v}$ , where  $\mathbf{v} = \mathbf{M}(\mathbf{M}^\top \mathbf{M})^{-1} \mathbf{p}$ . This result shows that, if we could exactly simulate the SDE (9), then the *marginal* distribution of the sample paths would converge to a measure  $\pi_{\mathbf{x}}$  on  $\mathcal{X}$  whose density is proportional to  $\exp(-\beta U(\mathbf{x}))$ . Therefore, for  $\beta = 1$  we would be sampling from  $\pi_{\mathcal{H}}$  (i.e. we recover SG-GMC), and for large  $\beta$ , we would be sampling near the global optimum of  $U$ .

## 4.3 Numerical integration

We will now develop an algorithm for simulating (9) in discrete-time. We follow the approach given in [BG13, LZS16], where we split (9) into three disjoint parts and solve those parts analytically in an iterative fashion. The split SDE is given as follows:

$$\text{A:} \begin{cases} d\tilde{\mathbf{x}}_t = \mathbf{G}^{-1} \mathbf{p}_t dt \\ d\mathbf{p}_t = \frac{1}{2} \nabla (\mathbf{p}_t^\top \mathbf{G}^{-1} \mathbf{p}_t) dt \end{cases} \quad \text{B:} \begin{cases} d\tilde{\mathbf{x}}_t = 0 \\ d\mathbf{p}_t = -c\mathbf{p}_t dt \end{cases} \quad \text{O:} \begin{cases} d\tilde{\mathbf{x}}_t = 0 \\ d\mathbf{p}_t = -(\nabla U_\lambda(\tilde{\mathbf{x}}_t) + \frac{1}{2} \nabla \log |\mathbf{G}|) dt \\ \quad \quad \quad + \sqrt{\frac{2c}{\beta} \mathbf{M}^\top \mathbf{M}} dW_t. \end{cases}$$



The nice property of these (stochastic) differential equations is that, each of them can be analytically simulated directly on the manifold  $\mathcal{X}$ , by using the identity  $\mathbf{x} = \xi(\tilde{\mathbf{x}})$  and the definitions of  $\mathbf{G}$ ,  $\mathbf{M}$ , and  $\mathbf{v}$ . In practice, one first needs to determine a sequence for the A, B, O steps, set a step-size  $h$  for integration along the time-axis  $t$ , and solve those steps one by one in an iterative fashion [LM15, CDC15]. In our applications, we have empirically observed that the sequence BOA provides better results among several other combinations, including the ABOBA scheme that was used in [LZS16]. We provide the solutions of the A, B, O steps, as well as the required gradients in the appendix.

#### 4.4 Theoretical analysis

In this section, we will provide non-asymptotic results for the proposed algorithm. Let us denote the output of the algorithm  $\{\mathbf{x}_k\}_{k=1}^N$ , where  $k$  denotes the iterations and  $N$  denotes the number of iterations. In the MAP estimation problem, we are interested in finding  $\mathbf{x}^* \triangleq \arg \min_{\mathbf{x}} U(\mathbf{x})$ , whereas for full Bayesian inference, we are interested in approximating posterior expectations with finite sample averages, i.e.  $\bar{\varphi} \triangleq \int_{\mathcal{X}} \varphi(\mathbf{x}) \pi_{\mathcal{H}}(\mathbf{x}) d\mathbf{x} \approx \hat{\varphi} \triangleq (1/N) \sum_{k=1}^N \varphi(\mathbf{x}_k)$ , where  $\varphi$  is a test function.

As briefly discussed in [LZS16], the convergence behavior of the SG-GMC algorithm can be directly analyzed within the theoretical framework presented in [CDC15]. In a nutshell, the theory in [CDC15] suggests that, with the BOA integration scheme, the bias  $|\mathbb{E}\hat{\varphi} - \varphi|$  is of order  $\mathcal{O}(N^{-1/2})$ .

In this study, we focus on the MAP estimation problem and analyze the *ergodic* error  $\mathbb{E}[\hat{U}_N - U^*]$ , where  $\hat{U}_N \triangleq (1/N) \sum_{k=1}^N U(\mathbf{x}_k)$  and  $U^* \triangleq U(\mathbf{x}^*)$ . This error resembles the bias where the test function  $\varphi$  is chosen as the potential  $U$ ; however, on the contrary, it directly relates the sample average to the global optimum. Similar ergodic error notions have already been considered in non-convex optimization [LHLL15, CCG<sup>+</sup>16].

We present our main result in the following theorem. In order to avoid obscuring the results, we present the required assumptions and the explicit forms of constants in the appendix. Briefly, the assumptions are mild and ensure the regularity of the potential  $U$  and the Markov process (9).

**Theorem 1.** *Assume that the conditions given in the appendix hold. If the iterates are obtained by using the BOA the scheme, then the following bound holds:*

$$|\mathbb{E}\hat{U}_N - U^*| = \mathcal{O}(\beta/(Nh) + h/\beta + 1/\beta), \quad (11)$$

for the domain  $\mathcal{X} = (\mathbb{S}^3)^n \times \mathbb{R}^{3n}$ .

*Proof (sketch).* The proof is based on decomposing the error into two terms:  $\mathbb{E}[\hat{U}_N - U^*] = \mathcal{A}_1 + \mathcal{A}_2$ , where  $\mathcal{A}_1 \triangleq \mathbb{E}[\hat{U}_N - \bar{U}_\beta]$  and  $\mathcal{A}_2 \triangleq [\bar{U}_\beta - U^*] \geq 0$ , and  $\bar{U}_\beta \triangleq \int_{\mathcal{X}} U(\mathbf{x}) \pi_{\mathbf{x}}(d\mathbf{x})$ . The term  $\mathcal{A}_1$  is the bias term, which we can bounded by using existing results. The rest of the proof deals with bounding  $\mathcal{A}_2$ , where we incorporate ideas from [RRT17]. The full proof is postponed to the appendix.  $\square$

Theorem 1 shows that the proposed algorithm will eventually provide samples that are close to the global optimizer  $\mathbf{x}^*$  even when  $U$  is non-convex. This result is stronger than the guarantees for the existing convex optimization algorithms on manifolds [ZS16, LSC<sup>+</sup>17], and is mainly due to the stochasticity of the algorithm that is introduced by the Brownian motion. However, despite this nice theoretical property, in practice our algorithm will still be affected by the *meta-stability phenomenon*, where it will converge near a local minimum and stay there for an exponential amount of time.

We note that our proof covers only the case where  $\mathcal{X} = (\mathbb{S}^3)^n \times \mathbb{R}^{3n}$ ; however, we believe that it can be easily extended to more general setting. We also note that the gradient computations in our algorithm can be replaced with stochastic gradients in the case of large-scale applications where the number of data points can be prohibitively large, so that computing the gradients at each iteration becomes practically infeasible. The same theoretical results hold as long as the stochastic gradients are unbiased.

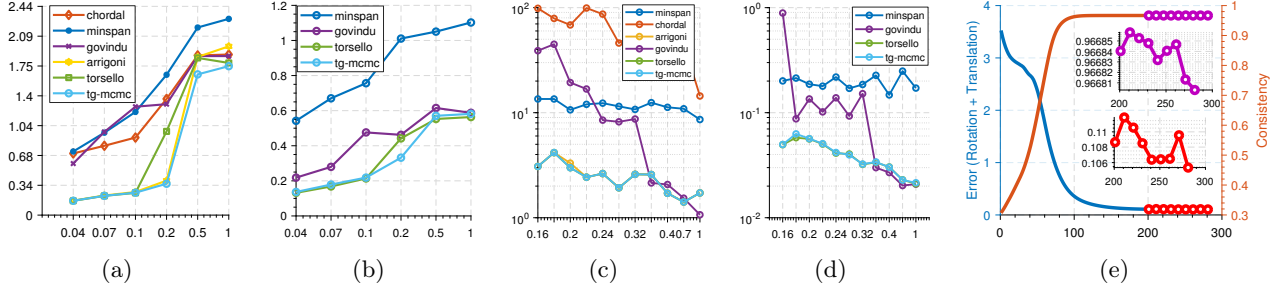


Figure 2: Synthetic Evaluations. (a) Noise variance vs mean Riemannian error. (b) Noise variance vs mean Euclidean (translational) error. (c)  $E\%$  vs Riemannian error for  $N = 50$ .  $E\%$  refers to graph completeness and  $N$  to the node count. (d)  $E\%$  vs Riemannian error for  $N = 50$ . (e) Monitoring the absolute error w.r.t. ground truth, during optimization and respective posterior sampling.

## 5 Experiments

We run a series of synthetic and real experiments to empirically show the characteristics of our algorithm. In a sequel of evaluations, we will be benchmarking our TG-MCMC against the state of the art methods including subsets of: convex programming of Ozyesil et. al. [OSB15], Lie algebraic method of Govindu [Gov04], dual quaternions linearization of Torsello et. al. [TRA11], direct EIG-SE3 method of Arrigoni [AFR15] and R-GODEC [AMR<sup>+</sup>14]. We also include two baseline methods: 1. propagating the pose information along one possible minimum spanning tree (minspan), 2. the chordal averaging [HTDL13] (chordal). We used the provided codes whenever possible.

**Hyper-parameter Selection** Throughout all the experiments we set  $c \leftarrow 1000$  and during optimization  $\beta \leftarrow \infty$ .  $h$  varies between 0.001 – 0.008 depending on the dataset. We typically set Bingham and Gaussian variances to be at the noise level of the dataset, evaluated empirically. Note that certain level of noise can also be compensated by the step size, as variance and step size are multiplicative factors. We initialize our algorithm randomly and Govindu [GP14, Gov04] from a minimum spanning tree (*minspan*).

**Graph Consistency** To give an intuitive measure of quantifying how well the estimated parameters agree to the input data, we propose *graph consistency* and define it as:

$$g_c = 1 - \frac{1}{\pi|E|} \sum_{(i,j) \in E} 2 \arccos(\mathbf{q}_{ij}(\mathbf{q}_i \bar{\mathbf{q}}_j)) \quad (12)$$

In other words,  $g_c$  measures how well the relative poses computed from absolute estimates align with the ones given in the data.  $g_c = 1$  for the perfect ground truth and  $g_c \rightarrow 0$  when all estimates are off by  $\pi$ . This measure is easier to interpret than, say, average rotational distance, that is always unit bound.

### 5.1 Synthetic Evaluations

We first synthesize random problems by drawing quaternions from Bingham and translations from Gaussian distributions, and randomly dropping edges from a fully connected pose graph. On these problems, we run a series of tests including monitoring the gradient steps, noise robustness, tolerance to graph completeness (sparsity) and fidelity w.r.t. ground truth. For each test, we distort the graph for the entity we test, i.e. add noise on nodes if we test the noise resilience.

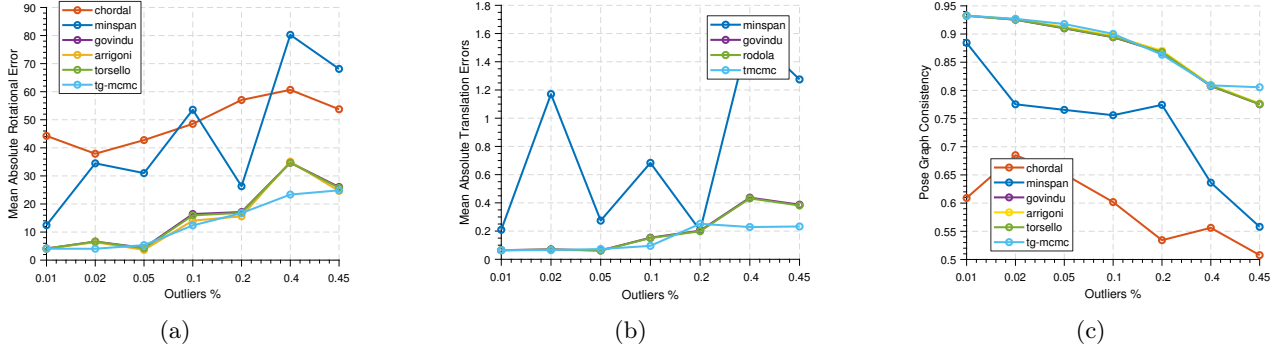


Figure 3: Robustness to outliers. With respect to the outlier percentage, we plot: (a) deviations of rotations from ground truth (mean error) (b) deviations of translation from ground truth (mean error) (c) graph consistency (for definition, see Equation 12).

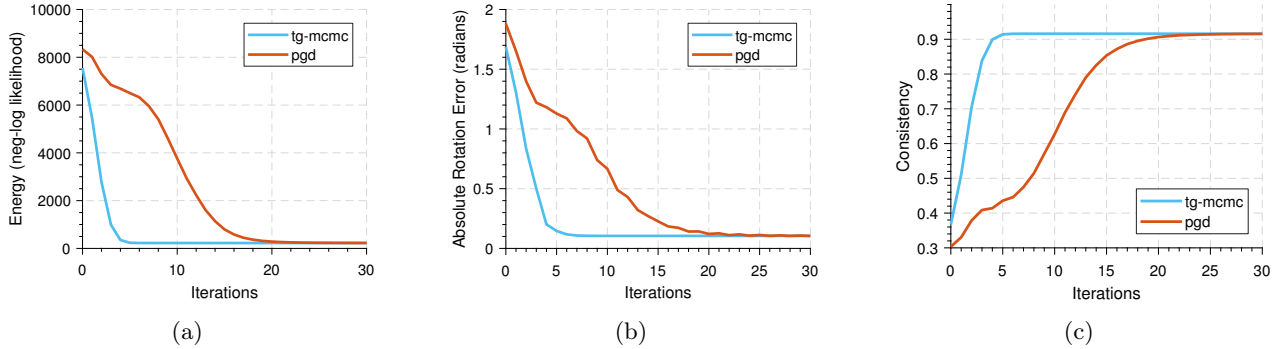


Figure 4: Synthetic evaluations against projected gradient descent (PGD). (a) Iterations vs negative log likelihood (b) Iterations vs absolute rotation error of the estimates w.r.t. ground truth. (c) Iterations vs consistency (for definition, see Equation 12).

### 5.1.1 Robustness to Noise

The rotational errors are evaluated by the true Riemannian distance,  $\|\log(\mathbf{R}^T \hat{\mathbf{R}})\|$ , the translations by Euclidean  $\|\mathbf{t} - \hat{\mathbf{t}}\|$ . Figure 2 plots our findings. It is noticeable that our accuracy is always on par with or better than the state of the art for moderate problems. In presence of significant degradation in the data, such as increased noise (Figures 2(a), 2(b)) or sparsified graph structure leading to missing data (Figures 2(c), 2(d)), our method shows clear advantage in both rotational and translational components of the error. This is thanks to our probabilistic formulation and theoretically grounded inference scheme.

### 5.1.2 Outlier Resilience

Even though TG-MCMC has no explicit treatment of outliers, it is still of interest to observe the robustness to outliers. We do that synthetically, by following a similar experimentation setup to the main paper. This time, we increase the outlier ratio in the pose graph by excessively corrupting some of the relative transformation matrices by composing it with random rotations in the range  $[60^\circ, 80^\circ]$  around random axes, and random translations between  $[0, 1]$ . We then run TG-MCMC, as well as the other algorithms under consideration. Our results are depicted in Figure 3. Many state-of-the-art methods that lack outlier handling are similar in performance. However, advantage of TG-MCMC is

Table 1: Evaluations on EPFL Benchmark [SVHVG<sup>+</sup>08].

	Ozyesil et. al.		R-GODEC		Govindu		Torsello		EIG-SE(3)		TG-MCMC	
	MRE	MTE	MRE	MTE	MRE	MTE	MRE	MTE	MRE	MTE	MRE	MTE
HerzJesus-P8	0.060	0.007	0.040	0.009	0.106	0.015	0.106	0.015	0.040	0.004	0.106	0.015
HerzJesus-P25	0.140	0.065	0.130	0.038	0.081	0.020	0.081	0.020	0.070	0.010	0.081	0.020
Fountain-P11	0.030	0.004	0.030	0.006	0.071	0.004	0.071	0.004	0.030	0.004	0.071	0.004
Entry-P10	0.560	0.203	0.440	0.433	0.101	0.035	0.101	0.035	0.040	0.009	0.090	0.035
Castle-P19	3.690	1.769	1.570	1.493	0.393	0.147	0.393	0.147	1.480	0.709	0.393	0.148
Castle-P30	1.970	1.393	0.780	1.123	0.631	0.323	0.629	0.321	0.530	0.212	0.622	0.285
Average	1.075	0.574	0.498	0.517	0.230	0.091	0.230	0.090	0.365	0.158	<b>0.227</b>	<b>0.085</b>

more apparent as the outlier percentage increases.

### 5.1.3 Projected Gradient Descent

Next, we compare our method against projected gradient descent (PGD) algorithm, that is heavily used when one avoids the manifold operations of quaternions. This amounts to solving our MAP estimation using a standard first order method and projecting the intermediary solutions back onto the manifold. Using compatible step sizes, Figure 4 plots multiple quantities as iterates progress. It is clearly visible that walking on the manifold is advantageous both in finding quicker solutions (a,b) and in reducing the energy of the cost (c).

## 5.2 Results in Real Data

We now evaluate our framework by running SFM on the EPFL Benchmark [SVHVG<sup>+</sup>08], that provide 8 to 30 images per dataset, along with ground-truth camera transformations. To quantify the accuracy, we match the ambiguous scale of the estimated translations to that of the ground truth, similar to [AFR15]. The mean rotation and translation errors (MRE, MTE) are depicted in Table 1. Notice that when rotations and translations are combined, our optimization results in superior minimum both for translations and orientations, not to mention the uncertainty information computed as a by-product. While many methods can perform similarly on easy sets, a clear advantage is visible on Castle sequences

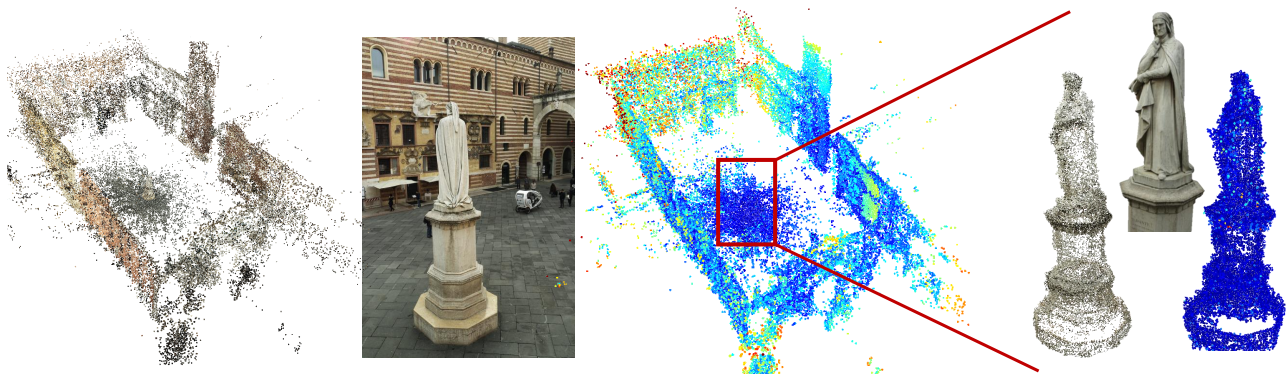


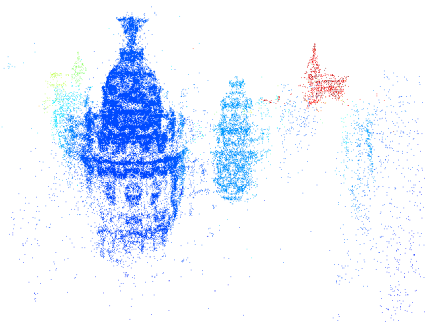
Figure 5: Uncertainty estimation in the Dante Square. From left to right: the colored reconstruction (bundle adjustment used in 3D structure only), a sample image from the dataset, reconstructed points colored w.r.t. uncertainty value, a close-up to the center of the square, Dante statue.



(a) Madrid Metropolis



(b) 3D Reconstruction

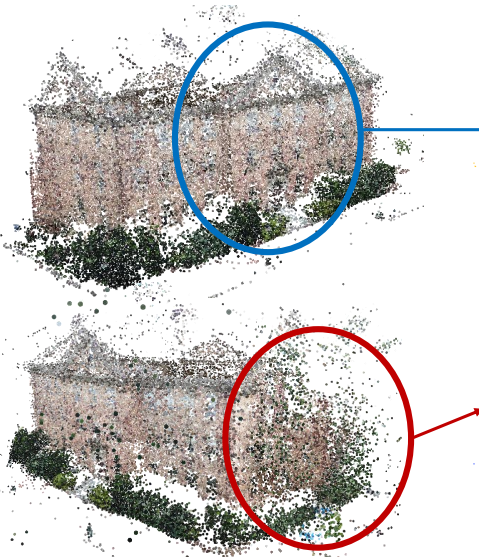


(c) Uncertainty Map

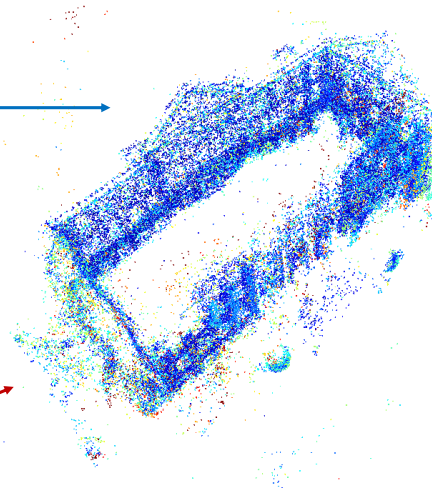
Figure 6: Reconstruction of Madrid Metropolis. Our uncertainty map can reveal the distant structure such as buildings because the 3D triangulation quality decreases with the distance. Samples produced by TG-MCMC can successfully explain these variations.



South Building



Reconstructions



Uncertainty Map

Figure 7: Reconstruction of South Building of UNC. Notice that hard-to-reconstruct structure such as vegetation is also marked to be uncertain by our algorithm, whereas rigid structures such as building façades enjoy high certainty.

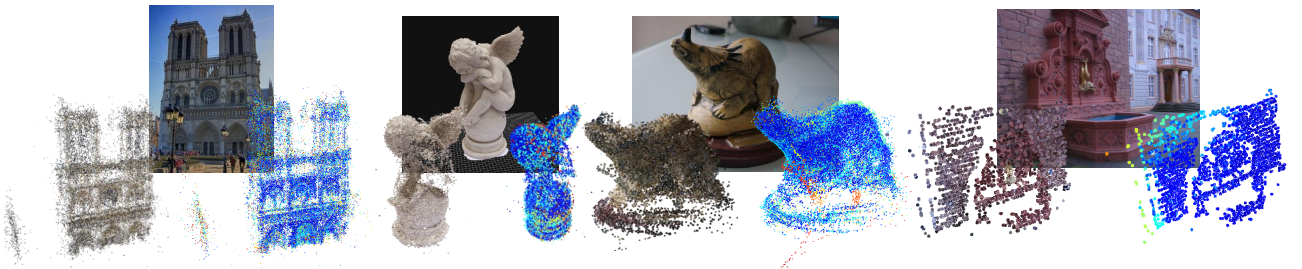


Figure 8: Visualization of uncertainty in Notre Dame, Angel, Dinosaur and Fountain datasets.

where severe noise and missing connections are present. There, for instance, EIG-SE(3) also fails to find a good closed form solution.

### 5.2.1 Uncertainty Estimation in Real Data

Estimating uncertainties within the same framework is a differentiating aspect of our method. Hence, we now qualitatively demonstrate the uncertainty estimation capabilities arising on various SFM problems and datasets [WS14, SVHVG<sup>+</sup>08]<sup>2</sup>. To do so, we first run our optimizer setting  $\beta \leftarrow \infty$  for  $> 400$  iterations. After that point, depending on the dataset, we set  $\beta$  to a finite value ( $\sim 1000$ ), allowing the sampling of posterior for 40 times. Similar behavior is shown in Figure 2(e). For each sample, that is a solution of the problem in Eq. 1, we perform a 3D reconstruction, similar to [CG13]: We first estimate 2D keypoints and relative rotations by running 1) VSFM [W<sup>+</sup>11] 2) two-frame bundle adjustment [AMO18] (BA) on image pairs, resulting in pairwise poses, as well as a rough two-view 3D structure. We run our method on these relative poses, computing the absolute estimates. Fixing the estimated poses, a second BA then optimizes for the optimal 3D structure. At the end, we obtain 40 3D scenes per dataset. For each point, we record the mean and variance across different reconstructions, transferring the uncertainty estimation to the 3D cloud of points. In figures 5, 6, 7 and 8, we colorize each point by mapping the uncertainty value to RGB space using a jet-colormap (blue lower, red higher), with a scale proportional to the diameter of reconstruction.

Figure 6 illustrates the uncertainty mapping on the Madrid Metropolis reconstruction and Figure 7 on the South Building dataset [SF16, SZPF16]. In the former, distant content, that is intrinsically less accurate to triangulate, appears less certain than the structure nearby. This overlaps well with the findings of stereo vision where baseline-to-distance ratio determines the triangulation accuracy. In the latter, though, we see that hard to match content such as vegetation has more uncertainty. This is also natural, because such image regions render the feature matching difficult. Finally, in Figure 8, we provide four more maps on Notre Dame, Angel, Dinosaur, and Fountain objects. In those, due to the noise and small size, variation is less apparent. Nevertheless, on Angel dataset, our algorithm overall manages to spot the noisy points and mark them with higher uncertainty. On the Fountain, the structure close to the borders of the scene are photographed from a fewer number of cameras, which is what TG-MCMC has discovered and on Notre Dame, and Dinosaur, outliers are picked to be uncertain.

### 5.2.2 Graph Evolution

To shade light upon the inner workings of TG-MCMC, we now visualize the evolution of the pose graph as iterations/time proceed(s) on the exemplary Angel object - see Figure 9. Notice, our algorithm can start from a random initialization and achieve results that are very close to the ground truth. In fact, we also show comparisons of the obtained pose graph against the ground truth poses in Figure 10. Our low numbers in quantitative error well transfers to qualitative evaluations.

## 6 Conclusion

We have proposed TG-MCMC, a manifold-aware, tempered rigid motion synchronization algorithm with a novel probabilistic formulation. TG-MCMC enjoys unique properties of trading-off approximately globally optimal solutions with non-asymptotic guarantees, to drawing samples from the posterior distribution, providing uncertainty estimates for the PGO-initialization problem. Our algorithm paves the way to a diverse potential future research: First, stochastic gradients can be employed to handle large problems, scaling up to hundreds of thousands of nodes. Next, the uncertainty estimates can be plugged into existing pipelines such as BA or PGO to further improve their quality. We also leave it as a future work to investigate different simulation schemes by altering the order of and combining differently the  $A$ ,  $B$  and  $O$  steps. Finally, TG-MCMC can be extended to different problems, still maintaining its nice theoretical properties.

---

<sup>2</sup>We also use 3D Flow datasets - <https://www.3dflow.net/3df-zephyr-reconstruction-showcase/>

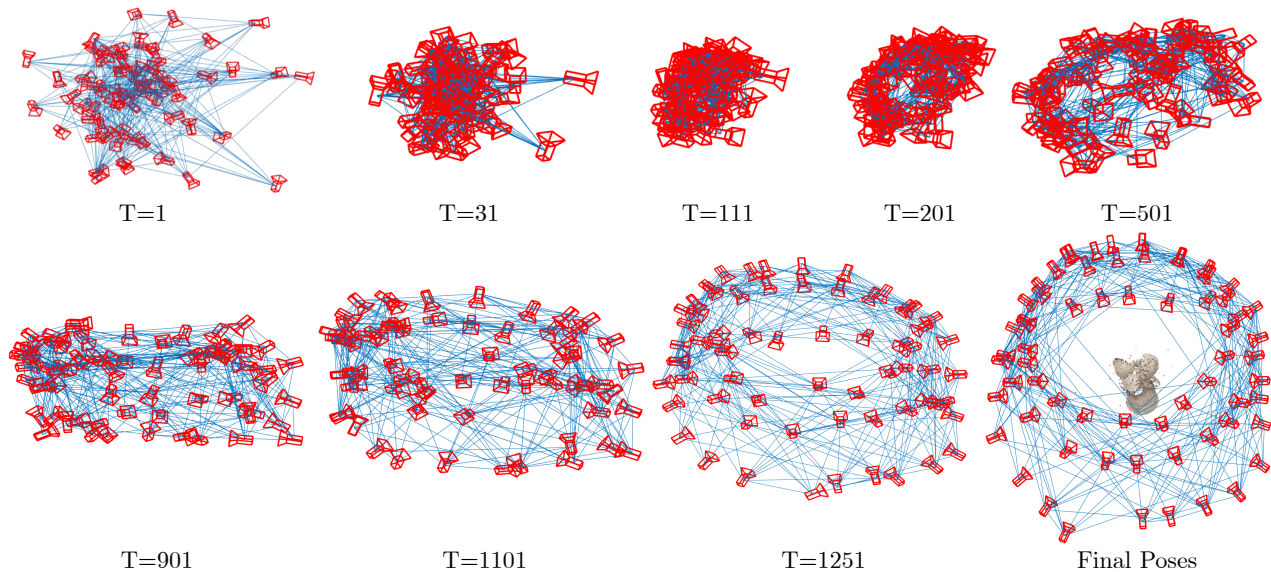


Figure 9: Evolution of the graph structure on the Angel object.  $T$  denotes iterations. TG-MCMC is initialized by random poses drawn from a Bingham distribution.

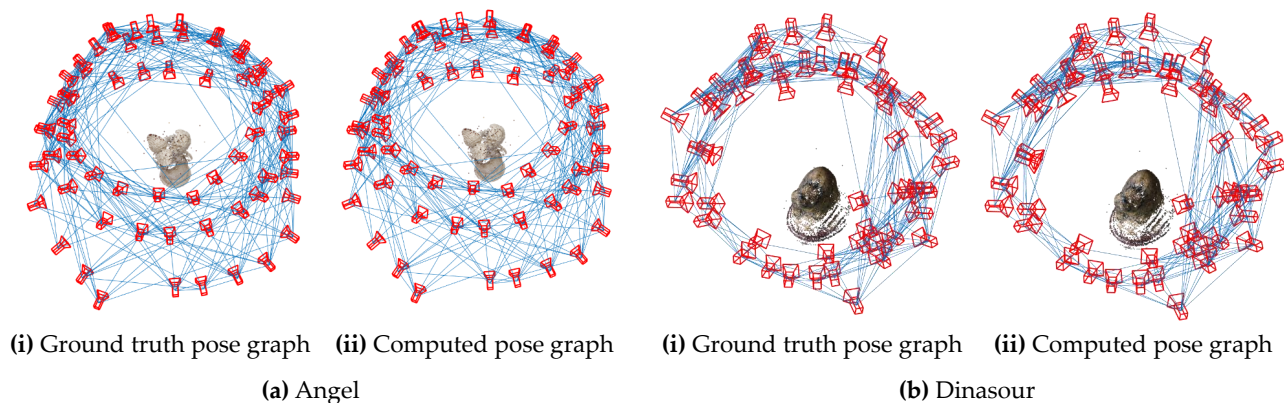


Figure 10: Comparing the resulting pose graph with the ground truth for Angel and Dino objects.

## References

- [AFR15] Federica Arrigoni, Andrea Fusiello, and Beatrice Rossi. Spectral motion synchronization in  $se(3)$ . *arXiv preprint arXiv:1506.08765*, 2015.
- [AFR16] Federica Arrigoni, Andrea Fusiello, and Beatrice Rossi. Camera motion from group synchronization. In *3D Vision (3DV), 2016 Fourth International Conference on*, pages 546–555. IEEE, 2016.
- [AMO18] Sameer Agarwal, Keir Mierle, and Others. Ceres solver. <http://ceres-solver.org>, 2018. Accessed: 2018-05-15.
- [AMR<sup>+</sup>14] Federica Arrigoni, Luca Magri, Beatrice Rossi, Pasqualina Fragneto, and Andrea Fusiello. Robust absolute rotation estimation via low-rank and sparse matrix decomposition. In *3D Vision (3DV), 2014 2nd International Conference on*, volume 1, pages 491–498. IEEE, 2014.

- [BG13] Simon Byrne and Mark Girolami. Geodesic monte carlo on embedded manifolds. *Scandinavian Journal of Statistics*, 40(4):825–845, 2013.
- [BGJ16] Jesus Briales and Javier Gonzalez-Jimenez. Fast global optimality verification in 3d slam. In *Intelligent Robots and Systems (IROS), 2016 IEEE/RSJ International Conference on*, pages 4630–4636. IEEE, 2016.
- [BGJ17] Jesus Briales and Javier Gonzalez-Jimenez. Initialization of 3d pose graph optimization using lagrangian duality. In *Robotics and Automation (ICRA), 2017 IEEE International Conference on*, pages 5134–5139. IEEE, 2017.
- [BI17] Tolga Birdal and Slobodan Ilic. Cad priors for accurate and flexible instance reconstruction. In *The IEEE International Conference on Computer Vision (ICCV)*, Oct 2017.
- [Bin74] Christopher Bingham. An antipodally symmetric distribution on the sphere. *The Annals of Statistics*, pages 1201–1225, 1974.
- [CC18] L. Carlone and G. C. Calafiore. Convex Relaxations for Pose Graph Optimization with Outliers. *ArXiv e-prints*, January 2018.
- [CCG<sup>+</sup>16] C. Chen, D. Carlson, Z. Gan, C. Li, and L. Carin. Bridging the gap between stochastic gradient MCMC and stochastic optimization. In *AISTATS*, 2016.
- [CDC15] C. Chen, N. Ding, and L. Carin. On the convergence of stochastic gradient MCMC algorithms with high-order integrators. In *Advances in Neural Information Processing Systems*, pages 2269–2277, 2015.
- [CG13] Avishek Chatterjee and Venu Madhav Govindu. Efficient and robust large-scale rotation averaging. In *Computer Vision (ICCV), 2013 IEEE International Conference on*, pages 521–528. IEEE, 2013.
- [CG18] Avishek Chatterjee and Venu Madhav Govindu. Robust relative rotation averaging. *IEEE transactions on pattern analysis and machine intelligence*, 40(4):958–972, 2018.
- [CTDD15] Luca Carlone, Roberto Tron, Kostas Daniilidis, and Frank Dellaert. Initialization techniques for 3d slam: a survey on rotation estimation and its use in pose graph optimization. In *Robotics and Automation (ICRA), 2015 IEEE International Conference on*, pages 4597–4604. IEEE, 2015.
- [DHS<sup>+</sup>13] Persi Diaconis, Susan Holmes, Mehrdad Shahshahani, et al. Sampling from a manifold. In *Advances in Modern Statistical Theory and Applications: A Festschrift in honor of Morris L. Eaton*, pages 102–125. Institute of Mathematical Statistics, 2013.
- [DX13] F. Dai and Y. Xu. *Approximation theory and harmonic analysis on spheres and balls*. Springer, 2013.
- [EOFC18] Anders Eriksson, Carl Olsson, Kahl Fredrik, and Tat-Jun Chin. Rotation averaging and strong duality. In *The IEEE Conference on Computer Vision and Pattern Recognition (CVPR)*, June 2018.
- [FO12] Johan Fredriksson and Carl Olsson. Simultaneous multiple rotation averaging using lagrangian duality. In *Asian Conference on Computer Vision*, pages 245–258. Springer, 2012.



- [GBR12] Jared Glover, Gary Bradski, and Radu Bogdan Rusu. Monte carlo pose estimation with quaternion kernels and the bingham distribution. In *Robotics: science and systems*, volume 7, page 97, 2012.
- [GK14] J. Glover and L. P. Kaelbling. Tracking the spin on a ping pong ball with the quaternion bingham filter. In *2014 IEEE International Conference on Robotics and Automation (ICRA)*, pages 4133–4140, May 2014.
- [GM91] S. B. Gelfand and S. K. Mitter. Recursive stochastic algorithms for global optimization in  $R^d$ . *SIAM Journal on Control and Optimization*, 29(5):999–1018, 1991.
- [Gov01] Venu Madhav Govindu. Combining two-view constraints for motion estimation. In *Computer Vision and Pattern Recognition, 2001. CVPR 2001. Proceedings of the 2001 IEEE Computer Society Conference on*, volume 2, pages II–II. IEEE, 2001.
- [Gov04] Venu Madhav Govindu. Lie-algebraic averaging for globally consistent motion estimation. In *Computer Vision and Pattern Recognition, 2004. CVPR 2004. Proceedings of the 2004 IEEE Computer Society Conference on*, volume 1, pages I–I. IEEE, 2004.
- [GP14] Venu Madhav Govindu and A Pooja. On averaging multiview relations for 3d scan registration. *IEEE Transactions on Image Processing*, 23(3):1289–1302, 2014.
- [Gra98] F Sebastian Grassia. Practical parameterization of rotations using the exponential map. *Journal of graphics tools*, 3(3):29–48, 1998.
- [HAT11] Richard Hartley, Khurram Aftab, and Jochen Trumpf. L1 rotation averaging using the weiszfeld algorithm. In *Computer Vision and Pattern Recognition (CVPR), 2011 IEEE Conference on*, pages 3041–3048. IEEE, 2011.
- [HH03] Daniel F Huber and Martial Hebert. Fully automatic registration of multiple 3d data sets. *Image and Vision Computing*, 21(7):637–650, 2003.
- [HTDL13] Richard Hartley, Jochen Trumpf, Yuchao Dai, and Hongdong Li. Rotation averaging. *International journal of computer vision*, 103(3):267–305, 2013.
- [Hwa80] C. Hwang. Laplace’s method revisited: weak convergence of probability measures. *The Annals of Probability*, pages 1177–1182, 1980.
- [KGJH13] Gerhard Kurz, Igor Gilitschenski, Simon Julier, and Uwe D Hanebeck. Recursive estimation of orientation based on the bingham distribution. In *Information Fusion (FUSION), 2013 16th International Conference on*, pages 1487–1494. IEEE, 2013.
- [KGS<sup>+</sup>11] Rainer Kümmerle, Giorgio Grisetti, Hauke Strasdat, Kurt Konolige, and Wolfram Burgard. g 2 o: A general framework for graph optimization. In *Robotics and Automation (ICRA), 2011 IEEE International Conference on*, pages 3607–3613. IEEE, 2011.
- [KPZK17] Arno Knapitsch, Jaesik Park, Qian-Yi Zhou, and Vladlen Koltun. Tanks and temples: Benchmarking large-scale scene reconstruction. *ACM Transactions on Graphics (TOG)*, 36(4):78, 2017.
- [KS09] D Karp and SM Sitnik. Inequalities and monotonicity of ratios for generalized hypergeometric function. *Journal of Approximation Theory*, 161(1):337–352, 2009.
- [KW07] Alfred Kume and Andrew TA Wood. On the derivatives of the normalising constant of the bingham distribution. *Statistics & probability letters*, 77(8):832–837, 2007.

- [LF<sup>+</sup>05] Vincent Lepetit, Pascal Fua, et al. Monocular model-based 3d tracking of rigid objects: A survey. *Foundations and Trends® in Computer Graphics and Vision*, 1(1):1–89, 2005.
- [LHLL15] X. Lian, Y. Huang, Y. Li, and J. Liu. Asynchronous parallel stochastic gradient for nonconvex optimization. In *Advances in Neural Information Processing Systems*, pages 2737–2745, 2015.
- [LM15] Ben Leimkuhler and Charles Matthews. *Molecular Dynamics: With Deterministic and Stochastic Numerical Methods*, volume 39. Springer, 2015.
- [LSC<sup>+</sup>17] Y. Liu, F. Shang, J. Cheng, H. Cheng, and L. Jiao. Accelerated first-order methods for geodesically convex optimization on Riemannian manifolds. In *Advances in Neural Information Processing Systems*, pages 4875–4884, 2017.
- [LZS16] Chang Liu, Jun Zhu, and Yang Song. Stochastic gradient geodesic mcmc methods. In *Advances in Neural Information Processing Systems*, pages 3009–3017, 2016.
- [MCF15] Y. A. Ma, T. Chen, and E. Fox. A complete recipe for stochastic gradient MCMC. In *Advances in Neural Information Processing Systems*, pages 2899–2907, 2015.
- [MF96] A Morawiec and DP Field. Rodrigues parameterization for orientation and misorientation distributions. *Philosophical Magazine A*, 73(4):1113–1130, 1996.
- [Mur94] Richard M Murray. *A mathematical introduction to robotic manipulation*. CRC press, 1994.
- [Nes13] Y. Nesterov. *Introductory lectures on convex optimization: A basic course*, volume 87. Springer Science & Business Media, 2013.
- [OSB15] Onur Ozyesil, Amit Singer, and Ronen Basri. Stable camera motion estimation using convex programming. *SIAM Journal on Imaging Sciences*, 8(2):1220–1262, 2015.
- [RCBL16] David M Rosen, Luca Carlone, Afonso S Bandeira, and John J Leonard. Se-sync: A certifiably correct algorithm for synchronization over the special euclidean group. *arXiv preprint arXiv:1612.07386*, 2016.
- [RRT17] M. Raginsky, A. Rakhlin, and M. Telgarsky. Non-convex learning via stochastic gradient Langevin dynamics: a nonasymptotic analysis. In *Proceedings of the 2017 Conference on Learning Theory*, volume 65, pages 1674–1703, 2017.
- [SF16] Johannes Lutz Schönberger and Jan-Michael Frahm. Structure-from-motion revisited. In *Conference on Computer Vision and Pattern Recognition (CVPR)*, 2016.
- [SK13] S. Sra and D. Karp. The multivariate Watson distribution: Maximum-likelihood estimation and other aspects. *Journal of Multivariate Analysis*, 114:256–269, 2013.
- [Ste51] Norman Earl Steenrod. *The topology of fibre bundles*, volume 14. Princeton University Press, 1951.
- [SVHVG<sup>+</sup>08] Christoph Strecha, Wolfgang Von Hansen, Luc Van Gool, Pascal Fua, and Ulrich Thoennessen. On benchmarking camera calibration and multi-view stereo for high resolution imagery. In *Computer Vision and Pattern Recognition, 2008. CVPR 2008. IEEE Conference on*, pages 1–8. Ieee, 2008.

- [SZPF16] Johannes Lutz Schönberger, Enliang Zheng, Marc Pollefeys, and Jan-Michael Frahm. Pixelwise view selection for unstructured multi-view stereo. In *European Conference on Computer Vision (ECCV)*, 2016.
- [TD14] Roberto Tron and Kostas Daniilidis. Statistical pose averaging with non-isotropic and incomplete relative measurements. In *European Conference on Computer Vision*, pages 804–819. Springer, 2014.
- [TLR18] Belinda Tzen, Tengyuan Liang, and Maxim Raginsky. Local optimality and generalization guarantees for the langevin algorithm via empirical metastability. In *Conference on Learning Theory*, 2018.
- [TMHF99] Bill Triggs, Philip F McLauchlan, Richard I Hartley, and Andrew W Fitzgibbon. Bundle adjustment—a modern synthesis. In *International workshop on vision algorithms*, pages 298–372. Springer, 1999.
- [TRA11] Andrea Torsello, Emanuele Rodola, and Andrea Albarelli. Multiview registration via graph diffusion of dual quaternions. In *Computer Vision and Pattern Recognition (CVPR), 2011 IEEE Conference on*, pages 2441–2448. IEEE, 2011.
- [TZD16] Roberto Tron, Xiaowei Zhou, and Kostas Daniilidis. A survey on rotation optimization in structure from motion. In *Proceedings of the IEEE Conference on Computer Vision and Pattern Recognition Workshops*, pages 77–85, 2016.
- [W<sup>+</sup>11] Changchang Wu et al. Visualsfm: A visual structure from motion system. 2011.
- [WBS16] Kyle Wilson, David Bindel, and Noah Snavely. When is rotations averaging hard? In *European Conference on Computer Vision*, pages 255–270. Springer, 2016.
- [WS14] Kyle Wilson and Noah Snavely. Robust global translations with 1dsfm. In *Proceedings of the European Conference on Computer Vision (ECCV)*, 2014.
- [ZLC17] Y. Zhang, P. Liang, and M. Charikar. A hitting time analysis of stochastic gradient langevin dynamics. In *Proceedings of the 2017 Conference on Learning Theory*, volume 65, pages 1980–2022, 2017.
- [ZS16] H. Zhang and S. Sra. First-order methods for geodesically convex optimization. In *Conference on Learning Theory*, pages 1617–1638, 2016.

## Appendix

### A Comparison to exponential coordinates

Many optimization algorithms tend to favor Rodrigues vector (exponential coordinates) [Mur94] parameterization due to  $R^3$  embedding and geodesics being straight lines [MF96]. This also leads to simpler Jacobian forms. In this paper, we argue that unit quaternions are more suitable for the approach we pursue: First, 3-vector formulations suffer from infinitely many singularities when the rotation angle approaches 0,  $\|\mathbf{a}\| \rightarrow 0$ , whereas quaternions avoid them [Gra98]. Moreover, quaternions have single redundancy in the representation  $\mathbf{q} = -\mathbf{q}$ , whereas the normed vectors possess infinite redundancy, i.e. the norm can grow indefinitely, but the angle lies in range  $[0 - 2\pi]$ . These make it harder to define continuous distributions directly on Rodrigues vectors. Yet, for quaternions there exists the natural antipodally symmetric Bingham distributions.

## B Numerical Integration

In this section, we provide the details of the numerical integration scheme that was explained in Section 4 of the main document. In short, the overall scheme is an extension of [LZS16], where we introduce the inverse temperature  $\beta$ .

Once the gradients with respect to the latent variables are computed, i.e.:

$$\nabla_{\mathbf{x}}U(\mathbf{x}) \equiv \{\nabla_{\mathbf{q}_1}U(\mathbf{x}), \dots, \nabla_{\mathbf{q}_n}U(\mathbf{x}), \nabla_{\mathbf{t}_1}U(\mathbf{x}), \dots, \nabla_{\mathbf{t}_n}U(\mathbf{x})\}, \quad (13)$$

we can update each of the variables  $\mathbf{q}_1, \dots, \mathbf{q}_n, \mathbf{t}_1, \dots, \mathbf{t}_n$  independently from each other, meaning that, the split integration steps, A, B, O can be applied to each of these variables independently. The operations A, B, O will differ depending on the manifold of the particular variable, therefore we will define these operations both on  $\mathbb{S}^3$  and  $\mathbb{R}^3$  for the two sets of variables  $\{\mathbf{q}_i\}_{i=1}^n$  and  $\{\mathbf{t}_i\}_{i=1}^n$ , respectively.

As we split  $\mathbf{x}$  into  $\{\mathbf{q}_i\}_{i=1}^n$  and  $\{\mathbf{t}_i\}_{i=1}^n$ , we similarly split the variable  $\mathbf{v}$  into  $\{\mathbf{v}_i^{\mathbf{q}}\}_{i=1}^n$  and  $\{\mathbf{v}_i^{\mathbf{t}}\}_{i=1}^n$  in order to facilitate the presentation.

### B.1 Update equations for the rotation components

Set a step-size  $h$ . For each  $\{\mathbf{q}_i, \mathbf{v}_i^{\mathbf{q}}\}$  pairs, the operations A, B, O have the following analytical form:

**Step A:**

Set  $\alpha = \|\mathbf{v}_i^{\mathbf{q}}\|$ ,  $\mathbf{q}' \leftarrow \mathbf{q}_i$  and  $\mathbf{v}' \leftarrow \mathbf{v}_i^{\mathbf{q}}$ .

$$\mathbf{q}_i \leftarrow \mathbf{q}' \cos(\alpha h) + (\mathbf{v}'/\alpha) \sin(\alpha h) \quad (14)$$

$$\mathbf{v}_i^{\mathbf{q}} \leftarrow -\alpha \mathbf{q}' \sin(\alpha h) + \mathbf{v}' \cos(\alpha h) \quad (15)$$

**Step B:**

$$\mathbf{v}_i^{\mathbf{q}} \leftarrow \exp(-ch) \mathbf{v}_i^{\mathbf{q}} \quad (16)$$

**Step O:**

Set  $\mathbf{v}' \leftarrow \mathbf{v}_i^{\mathbf{q}}$  and  $\mathbf{g} \leftarrow \nabla_{\mathbf{q}_i}U(\mathbf{x})$

$$\mathbf{v}_i^{\mathbf{q}} \leftarrow \mathbf{v}' + P(\mathbf{q}_i)(-h\mathbf{g} + \sqrt{2c/\beta} \mathbf{z}_i^{\mathbf{q}}), \quad (17)$$

where  $P(\mathbf{q}) = (\mathbf{I} - \mathbf{q}\mathbf{q}^\top)$  denotes the projector and  $\mathbf{z}_i^{\mathbf{q}}$  denotes a standard Gaussian random variable on  $\mathbb{R}^4$ .

### B.2 Update equations for the translation components

Set a step-size  $h$ . For each  $\{\mathbf{t}_i, \mathbf{v}_i^{\mathbf{t}}\}$  pairs, the operations A, B, O have the following analytical form:

**Step A:**

$$\mathbf{q}_i \leftarrow \mathbf{q}_i + h\mathbf{v}_i^{\mathbf{t}} \quad (18)$$

**Step B:**

$$\mathbf{v}_i^{\mathbf{t}} \leftarrow \exp(-ch) \mathbf{v}_i^{\mathbf{t}} \quad (19)$$

**Step O:**

Set  $\mathbf{v}' \leftarrow \mathbf{v}_i^t$  and  $\mathbf{g} \leftarrow \nabla_{\mathbf{t}_i} U(\mathbf{x})$

$$\mathbf{v}_i^t \leftarrow \mathbf{v}' + (-h\mathbf{g} + \sqrt{2c/\beta}\mathbf{z}_i^t), \quad (20)$$

where  $\mathbf{z}_i^t$  denotes a standard Gaussian random variable on  $\mathbb{R}^3$ .

### B.3 Algorithm pseudocode

We illustrate the overall algorithm in Algorithm 1. Note that as the updates of  $\mathbf{q}$  do not depend on  $\mathbf{t}$ , we can separate the updates and use the up to date values of orientations, for computing the translations.

---

**Algorithm 1:** TG-MCMC

---

```

1 input :  $\mathbf{x}_0 = \{\mathbf{q}_1, \dots, \mathbf{q}_n, \mathbf{t}_1, \dots, \mathbf{t}_n\}$ ,  $\mathbf{v} = \{\mathbf{v}_1^q, \dots, \mathbf{v}_n^q, \mathbf{v}_1^t, \dots, \mathbf{v}_n^t\}$ ,  $\beta, c, h$ 
2 for  $i = 1, \dots, N$  do
3   Compute the gradient  $\nabla_{\mathbf{x}} U(\mathbf{x}_i)$ 
4   // Update the rotation components
5   for  $j = 1, \dots, n$  do
6     Run the B, O, A steps (in this order) on  $\mathbf{q}_j, \mathbf{v}_j^q$  (Section B.1)
7   // Update the translation components
8   for  $j = 1, \dots, n$  do
9     Run the B, O, A steps (in this order) on  $\mathbf{t}_j, \mathbf{v}_j^t$  (Section B.2)

```

---

## C Assumptions

In this section, we state the assumptions that imply our theoretical results.

**H1.** *The gradient of the potential is Lipschitz continuous, i.e. there exists  $L < \infty$ , such that  $\|\nabla_{\mathbf{x}} U(\mathbf{x}) - \nabla_{\mathbf{x}} U(\mathbf{x}')\| \leq L d_{\mathcal{X}}(\mathbf{x}, \mathbf{x}')$ ,  $\forall \mathbf{x}, \mathbf{x}' \in \mathcal{X}$ , where  $d_{\mathcal{X}}$  denotes the geodesic distance on  $\mathcal{X}$ .*

**H2.** *The second-order moments of  $\pi_{\mathbf{x}}$  are bounded and satisfies the following inequality:  $\int_{\mathbb{R}^d} \|\mathbf{x}\|^2 \pi_{\mathbf{x}}(d\mathbf{x}) \leq \frac{C}{\beta}$ , for some  $C > 0$ .*

**H3.** *Let  $\psi$  be a functional that is the unique solution of a Poisson equation that is defined as follows:*

$$\mathcal{L}_n \psi(\varphi_n) = U(\mathbf{x}_n) - \bar{U}_\beta, \quad (21)$$

where  $\varphi_n = [\tilde{\mathbf{x}}_n^\top, \mathbf{p}_n^\top]^\top$ ,  $\mathcal{L}_n$  is the generator of (9) at  $t = nh$  (see [CDC15] for the definition). The functional  $\psi$  and its up to third-order derivatives  $\mathcal{D}^k \psi$  are bounded by a function  $V(\varphi)$ , such that  $\|\mathcal{D}^k \psi\| \leq C_k V^{r_k}$  for  $k = 0, 1, 2, 3$  and  $C_k, r_k > 0$ . Furthermore,  $\sup_n \mathbb{E} V^r(\mathbf{x}_n) < \infty$  and  $V$  is smooth such that  $\sup_{s \in (0,1)} V^r(s\varphi + (1-s)\varphi') \leq C(V^r(\varphi) + V^r(\varphi'))$  for all  $\varphi, \varphi' \in \mathbb{R}^{12n}$ ,  $r \leq \max 2r_k$ , and  $C > 0$ .

## D Proof of Proposition 1

*Proof.* We start by rewriting the SDE given in (9) as follows:

$$d\varphi_t = \left\{ - \left( \underbrace{\begin{bmatrix} 0 & 0 \\ 0 & \frac{c\mathbf{M}^\top \mathbf{M} \mathbf{I}}{\beta} \end{bmatrix}}_{\mathbf{D}} + \underbrace{\begin{bmatrix} 0 & -\frac{\mathbf{I}}{\beta} \\ \frac{\mathbf{I}}{\beta} & 0 \end{bmatrix}}_{\mathbf{Q}} \right) \underbrace{\begin{bmatrix} \mathcal{A}(\tilde{\mathbf{x}}_t, \mathbf{p}_t, \beta) \\ \beta \mathbf{G}^{-1} \mathbf{p}_t \end{bmatrix}}_{\nabla_{\varphi} \mathcal{E}_{\lambda}(\varphi_t)} \right\} dt + \sqrt{2\mathbf{D}} dW_t. \quad (22)$$

where  $\mathcal{A}(\tilde{\mathbf{x}}_t, \mathbf{p}_t, \beta) \triangleq \beta \nabla_{\tilde{\mathbf{x}}} U_{\lambda}(\tilde{\mathbf{x}}_t) + \frac{\beta}{2} \nabla_{\tilde{\mathbf{x}}} \log |\mathbf{G}| + \frac{\beta}{2} \nabla_{\tilde{\mathbf{x}}} (\mathbf{p}_t^\top \mathbf{G}^{-1} \mathbf{p}_t)$ . Here, we observe that  $\mathbf{D}$  is positive semi-definite,  $\mathbf{Q}$  is anti-symmetric. Then, the desired result is a direct consequence of Theorem 1 of [MCF15].  $\square$

## E Proof of Theorem 1

Before proving Theorem 1, we first prove the following intermediate results, whose proofs are given later in this document.

**Corollary 1.** *Assume that **H1** and **H3** hold. Let  $\{\mathbf{x}_n, \mathbf{v}_n\}$  be the output our algorithm with  $\beta > 0$ . Define  $\hat{U}_N \triangleq \frac{1}{N} \sum_{n=1}^N U(\mathbf{x}_n)$ . Then the following bound holds for the bias:*

$$|\mathbb{E} \hat{U}_N - \bar{U}_{\beta}| = \mathcal{O}\left(\frac{\beta}{Nh} + \frac{h}{\beta}\right). \quad (23)$$

**Lemma 1.** *Assume that the conditions **H1** and **H2** hold. Then, the following bound holds for  $\beta \leq \frac{6}{L\pi^2} \log \frac{CL\pi^3 e}{3\Gamma(3/2)^{2/3_n}}$ :*

$$\bar{U}_{\beta} - U^* = \mathcal{O}\left(\frac{1}{\beta}\right), \quad (24)$$

where  $C$  is defined in **H2**.

*Proof of Theorem 1.* The proof is a direct application of Corollary 1 and Lemma 1.  $\square$

## F Proof of Corollary 1

*Proof.* From [CDC15][Theorem 2], the bias of a standard SG-MCMC algorithm (i.e.  $\beta = 1$ ) is bounded by

$$\mathcal{O}\left(\frac{1}{Nh'} + \frac{\sum_{n=1}^N \|\mathbb{E} \Delta V_n\|}{N} + h'\right). \quad (25)$$

where  $h'$  denotes the step-size and  $\Delta V_n$  is an operator and it is related to bias of the stochastic gradient computations if there is any. If the iterates are obtained via full gradient computations  $\nabla U$  or unbiased stochastic gradients computations (i.e. the case we consider here), then we have  $\|\mathbb{E} \Delta V_n\| = 0$ . Then by using a time-scaling argument similar to [RRT17, ZLC17], we define  $h = \frac{h'}{\beta}$ . This corresponds to running a standard SG-MCMC algorithm directly on the energy function  $\mathcal{E}_{\mathcal{H}}(\mathbf{x}, \mathbf{v})$ . The result is then obtained by replacing  $h'$  by  $\frac{h}{\beta}$  in (25).  $\square$

## G Proof of Lemma 1

In order to prove Lemma 1, we first need some rather elementary technical results, which we provide in Section H for clarity.

*Proof.* We use a similar proof technique to the one given in [RRT17][Proposition 11]. We assume that  $\pi_{\mathbf{x}}$  admits a density, denoted as  $\rho(\mathbf{x}) \triangleq \frac{1}{Z_\beta} \exp(-\beta U(\mathbf{x}))$ , where  $Z_\beta$  is the normalization constant:

$$Z_\beta \triangleq \int_{\mathcal{X}} \exp(-\beta U(\mathbf{x})) d\mathbf{x}. \quad (26)$$

We start by using the definition of  $\bar{U}_\beta$ , as follows:

$$\bar{U}_\beta = \int_{\mathcal{X}} U(\mathbf{x}) \pi_{\mathbf{x}}(d\mathbf{x}) = \frac{1}{\beta} (H(\rho) - \log Z_\beta), \quad (27)$$

where  $H(\rho)$  is the *differential entropy*, defined as follows:

$$H(\rho) \triangleq - \int_{\mathcal{X}} \rho(\mathbf{x}) \log \rho(\mathbf{x}) d\mathbf{x}. \quad (28)$$

We now aim at upper-bounding  $H(\rho)$  and lower-bounding  $\log Z_\beta$ .

By Assumption **H2**, the distribution  $\pi_{\mathbf{x}}$  has a finite second-order moment, therefore all the marginal distributions will also have bounded second order moments. By abusing the notation and denoting  $\mathbf{x} \equiv \{\mathbf{q}_1, \dots, \mathbf{q}_n, \mathbf{t}_1, \dots, \mathbf{t}_n\}$ , and by using the fact that the joint differential entropy is smaller than the sum of the differential entropies of the individual random variables, we can upper-bound  $H(\rho)$  as follows:

$$H(\rho) \leq \sum_{i=1}^n H(\rho_{\mathbf{q}_i}) + H(\rho_{\mathbf{t}_1, \dots, \mathbf{t}_n}), \quad (29)$$

where  $\rho_{\mathbf{q}_i}$  denotes the marginal density of  $\mathbf{q}_i$  and  $\rho_{\mathbf{t}_1, \dots, \mathbf{t}_n}$  denotes the joint marginal density of  $(\mathbf{t}_1, \dots, \mathbf{t}_n)$ . Since  $\rho_{\mathbf{t}_1, \dots, \mathbf{t}_n}$  is defined on  $\mathbb{R}^{3n}$ , we know that  $H(\rho_{\mathbf{t}_1, \dots, \mathbf{t}_n})$  is upper-bounded by the differential entropy of a Gaussian distribution on  $\mathbb{R}^{3n}$  that has the same second order moment. By denoting the covariance matrix of the Gaussian distribution with  $\Sigma$ , we obtain:

$$\mathcal{H}(\rho_{\mathbf{t}_1, \dots, \mathbf{t}_n}) \leq \frac{1}{2} \log[(2\pi e)^{3n} \det(\Sigma)] \quad (30)$$

$$\leq \frac{1}{2} \log[(2\pi e)^{3n} \left(\frac{\text{tr}(\Sigma)}{3n}\right)^{3n}] \quad (31)$$

$$\leq \frac{3n}{2} \log\left(2\pi e \frac{C}{3\beta n}\right), \quad (32)$$

The equations (31) and (32) follows by the relation between the arithmetic and geometric means, and Assumption **H2**.

By using a similar argument, since  $\rho_{\mathbf{q}_i}$  lives on the unit sphere, its differential entropy is upper-bounded by the differential entropy of the uniform distribution on the unit sphere. Accordingly, we obtain:

$$H(\rho_{\mathbf{q}_i}) \leq \log\left(\frac{(2\pi)^{3/2}}{\Gamma(3/2)}\right), \quad (33)$$

where  $\Gamma(\cdot)$  denotes the gamma function. By using (32) and (33) in (29), we obtain

$$H(\rho) \leq n \log\left(\frac{(2\pi)^{3/2}}{\Gamma(3/2)}\right) + \frac{3n}{2} \log\left(2\pi e \frac{C}{3\beta n}\right) \quad (34)$$

$$= \frac{3n}{2} \log\left(\frac{2\pi}{\Gamma(3/2)^{2/3}}\right) + \frac{3n}{2} \log\left(2\pi e \frac{C}{3\beta n}\right) \quad (35)$$

$$= \frac{3n}{2} \log\left(\frac{4\pi^2 e C}{3\Gamma(3/2)^{2/3} \beta n}\right). \quad (36)$$

We now lower-bound  $\log Z_\beta$ . By definition, we have

$$\log Z_\beta = \log \int_{\mathcal{X}} \exp(-\beta U(\mathbf{x})) d\mathbf{x} \quad (37)$$

$$= -\beta U^* + \log \int_{\mathcal{X}} \exp(\beta(U^* - U(\mathbf{x}))) d\mathbf{x} \quad (38)$$

$$\geq -\beta U^* + \log \int_{\mathcal{X}} \exp\left(-\frac{\beta L \pi^2 \|\mathbf{x} - \mathbf{x}^*\|^2}{8}\right) d\mathbf{x} \quad (39)$$

Here, in (39) we used Assumption **H1** and Corollary 2 (presented below). By using  $\mathbf{x} \equiv [\mathbf{q}_1^\top, \dots, \mathbf{q}_n^\top, \mathbf{t}^\top]^\top$  and  $\mathbf{x}^* \equiv [(\mathbf{q}_1^*)^\top, \dots, (\mathbf{q}_n^*)^\top, (\mathbf{t}^*)^\top]^\top$ , and  $\mathbf{t} \equiv [\mathbf{t}_1^\top, \dots, \mathbf{t}_n^\top]^\top$ ,  $\mathbf{t}^* \equiv [(\mathbf{t}_1^*)^\top, \dots, (\mathbf{t}_n^*)^\top]^\top$  we obtain:

$$\begin{aligned} \log Z_\beta &\geq -\beta U^* + \log\left(\prod_{i=1}^n \int_{\mathbb{S}^3} \exp\left(-\frac{\beta L \pi^2 \|\mathbf{q}_i - \mathbf{q}_i^*\|^2}{8}\right) d\mathbf{q}_i\right) \\ &\quad + \log\left(\int_{\mathbb{R}^{3n}} \exp\left(-\frac{\beta L \pi^2 \|\mathbf{t} - \mathbf{t}^*\|^2}{8}\right) d\mathbf{t}\right) \end{aligned} \quad (40)$$

$$\begin{aligned} &= -\beta U^* + \log\left(\prod_{i=1}^n \int_{\mathbb{S}^3} \exp\left(-\frac{\beta L \pi^2 \|\mathbf{q}_i - \mathbf{q}_i^*\|^2}{8}\right) d\mathbf{q}_i\right) \\ &\quad + \frac{3n}{2} \log\left(\frac{4}{\beta L \pi}\right). \end{aligned} \quad (41)$$

Let us focus on the integral with respect to  $\mathbf{q}_i$ . By definition, we have:

$$\int_{\mathbb{S}^3} \exp\left(-\frac{\beta L \pi^2 \|\mathbf{q}_i - \mathbf{q}_i^*\|^2}{8}\right) d\mathbf{q}_i = \int_{\mathbb{S}^3} \exp\left(-\frac{\beta L \pi^2}{8} (2 - 2\mathbf{q}_i^\top \mathbf{q}_i^*)\right) d\mathbf{q}_i \quad (42)$$

$$= \exp\left(-\frac{\beta L \pi^2}{4}\right) \int_{\mathbb{S}^3} \exp\left(\frac{\beta L \pi^2}{4} \mathbf{q}_i^\top \mathbf{q}_i^*\right) d\mathbf{q}_i. \quad (43)$$

By using the connection between the integral on the right hand side of the above equation and multivariate Watson's distribution (see Equations 2.1 and 2.2 in [SK13]), we obtain:

$$\int_{\mathbb{S}^3} \exp\left(-\frac{\beta L \pi^2 \|\mathbf{q}_i - \mathbf{q}_i^*\|^2}{8}\right) d\mathbf{q}_i = \exp\left(-\frac{\beta L \pi^2}{4}\right) 2\pi^2 M\left(\frac{1}{2}, 2, \frac{\beta L \pi^2}{4}\right), \quad (44)$$

where  $M$  denotes the Kummer confluent hypergeometric function that is defined as follows:

$$M(a, b, c) \triangleq \sum_{j=0}^{\infty} \frac{a^{\bar{j}} c^j}{b^{\bar{j}} j!}, \quad (45)$$



where  $a^{\bar{0}} \triangleq 1$  and  $a^{\bar{j}} \triangleq a(a+1)\dots(a+j-1)$  for  $j \geq 1$ . By Theorem 3 of [KS09], we know that

$$M\left(\frac{1}{2}, 2, \frac{\beta L \pi^2}{4}\right) \geq \frac{1}{1 + \frac{\beta L \pi^2}{16}} = \frac{16}{16 + \beta L \pi^2}. \quad (46)$$

By using this inequality in (44), we obtain:

$$\int_{\mathbb{S}^3} \exp\left(-\frac{\beta L \pi^2 \|\mathbf{q}_i - \mathbf{q}_i^*\|^2}{8}\right) d\mathbf{q}_i \geq \exp\left(-\frac{\beta L \pi^2}{4}\right) \frac{32\pi^2}{16 + \beta L \pi^2}. \quad (47)$$

We can insert (47) in (41), as follows:

$$\log Z_\beta \geq -\beta U^* + \frac{3n}{2} \log\left(\frac{4}{\beta L \pi}\right) + \sum_{i=1}^n \log \int_{\mathbb{S}^3} \exp\left(-\frac{\beta L \pi^2 \|\mathbf{q}_i - \mathbf{q}_i^*\|^2}{8}\right) d\mathbf{q}_i \quad (48)$$

$$\geq -\beta U^* + \frac{3n}{2} \log\left(\frac{4}{\beta L \pi}\right) - n \frac{\beta L \pi^2}{4} + n \log \frac{32\pi^2}{16 + \beta L \pi^2} \quad (49)$$

$$\geq -\beta U^* + \frac{3n}{2} \log\left(\frac{4}{\beta L \pi}\right) - n \frac{\beta L \pi^2}{4} \quad (50)$$

Finally, by combining (27), (36), and (50), we obtain:

$$\bar{U}_\beta - U^* = \frac{1}{\beta} (\mathcal{H}(\rho) - \log Z_\beta) - U^* \quad (51)$$

$$\leq \frac{3n}{2\beta} \log\left(\frac{4\pi^2 e C}{3\Gamma(3/2)^{2/3} \beta n}\right) - \frac{3n}{2\beta} \log\left(\frac{4}{\beta L \pi}\right) + n \frac{L\pi^2}{4} \quad (52)$$

$$= \frac{3n}{2\beta} \log\left(\frac{CL\pi^3 e}{3\Gamma(3/2)^{2/3} n}\right) + n \frac{L\pi^2}{4} \quad (53)$$

$$\leq \frac{3n}{\beta} \log\left(\frac{CL\pi^3 e}{3\Gamma(3/2)^{2/3} n}\right). \quad (54)$$

The last line follows from the hypothesis. This finalizes the proof.  $\square$

## H Technical Results

In the following lemma, we generalize [Nes13][Lemma 1.2.3] to manifolds. Similar arguments can be found in [ZS16, LSC<sup>+</sup>17].

**Lemma 2.** *Let  $\mathcal{X} \subset \mathbb{R}^n$  be a Riemannian manifold with metric  $d_{\mathcal{X}}$ , and let  $\gamma : [0, 1] \mapsto \mathcal{X}$  be a constant-speed geodesic curve between two points  $\mathbf{x}, \mathbf{y} \in \mathcal{X}$ , such that  $\gamma(0) = \mathbf{x}$  and  $\gamma(1) = \mathbf{y}$ . Let  $f : \mathcal{X} \mapsto \mathbb{R}$  be a continuously differentiable function with Lipschitz continuous gradients. Then the following bound holds for every  $\mathbf{x}, \mathbf{y} \in \mathcal{X}$ :*

$$\left| f(\mathbf{y}) - f(\mathbf{x}) - \int_0^1 \langle \nabla f(\mathbf{x}), \gamma'(t) \rangle dt \right| \leq \frac{L}{2} d_{\mathcal{X}}(\mathbf{x}, \mathbf{y})^2, \quad (55)$$

where  $\langle \mathbf{x}, \mathbf{y} \rangle \triangleq \mathbf{x}^\top \mathbf{y}$  and  $L$  denotes the Lipschitz constant.

*Proof.* Let us define a function  $\varphi : [0, 1] \mapsto \mathbb{R}$ , such that  $\varphi(t) \triangleq f(\gamma(t))$ . By definition, we have  $\varphi(0) = f(\mathbf{x})$  and  $\varphi(1) = f(\mathbf{y})$ . By using the second fundamental theorem of calculus, we can write:

$$\varphi(1) - \varphi(0) = \int_0^1 \varphi'(t) dt, \quad (56)$$

where  $\varphi'(t)$  denotes the derivative of  $\varphi(t)$  with respect to  $t$ . By the theorem of derivation of composite functions, we have

$$\varphi'(t) = \langle \nabla f(\gamma(t)), \gamma'(t) \rangle. \quad (57)$$

By combining (56) and (57), we obtain the following identity for all  $\mathbf{x}, \mathbf{y} \in \mathcal{X}$ :

$$f(\mathbf{y}) = f(\mathbf{x}) + \int_0^1 \langle \nabla f(\gamma(t)), \gamma'(t) \rangle dt \quad (58)$$

$$= f(\mathbf{x}) + \int_0^1 \langle \nabla f(\mathbf{x}), \gamma'(t) \rangle dt + \int_0^1 \langle \nabla f(\gamma(t)) - \nabla f(\mathbf{x}), \gamma'(t) \rangle dt. \quad (59)$$

Therefore, we obtain

$$\left| f(\mathbf{y}) - f(\mathbf{x}) - \int_0^1 \langle \nabla f(\mathbf{x}), \gamma'(t) \rangle dt \right| = \left| \int_0^1 \langle \nabla f(\gamma(t)) - \nabla f(\mathbf{x}), \gamma'(t) \rangle dt \right| \quad (60)$$

$$\leq \int_0^1 \left| \langle \nabla f(\gamma(t)) - \nabla f(\mathbf{x}), \gamma'(t) \rangle \right| dt \quad (61)$$

$$\leq \int_0^1 \|\nabla f(\gamma(t)) - \nabla f(\mathbf{x})\| \|\gamma'(t)\| dt \quad (62)$$

$$\leq L \int_0^1 d_{\mathcal{X}}(\gamma(t), \mathbf{x}) \|\gamma'(t)\| dt. \quad (63)$$

We can now use the fact that the geodesic curve has a constant velocity, such that  $\|\gamma'(t)\| = d_{\mathcal{X}}(\mathbf{x}, \mathbf{y})$  for all  $t \in [0, 1]$ , which also implies  $d_{\mathcal{X}}(\gamma(t_1), \gamma(t_2)) = |t_1 - t_2| d_{\mathcal{X}}(\gamma(1), \gamma(0))$ . Then, using  $\mathbf{x} = \gamma(0)$ ,  $\mathbf{y} = \gamma(1)$ , we obtain:

$$\left| f(\mathbf{y}) - f(\mathbf{x}) - \int_0^1 \langle \nabla f(\mathbf{x}), \gamma'(t) \rangle dt \right| \leq L \int_0^1 t d_{\mathcal{X}}(\mathbf{x}, \mathbf{y})^2 dt \quad (64)$$

$$= \frac{L}{2} d_{\mathcal{X}}(\mathbf{x}, \mathbf{y})^2. \quad (65)$$

This concludes the proof.  $\square$

**Corollary 2.** *Under the assumptions of Lemma 2, the following bound holds for all  $\mathbf{x} \in \mathcal{X}$*

$$f(\mathbf{x}) - f^* \leq \frac{L\pi^2}{8} \|\mathbf{x} - \mathbf{x}^*\|^2, \quad (66)$$

where  $\mathcal{X} \triangleq (\mathbb{S}^3)^n \times \mathbb{R}^{3n}$ ,  $f^* = \min_{\mathbf{x}' \in \mathcal{X}} f(\mathbf{x}')$  and  $\mathbf{x}^* = \arg \min_{\mathbf{x}' \in \mathcal{X}} f(\mathbf{x}')$ .

*Proof.* By using Lemma 2 and the obvious facts that  $\nabla f(\mathbf{x}^*) = 0$  and  $f(\mathbf{x}) > f^*$  for all  $\mathbf{x} \in \mathcal{X}$ , we have:

$$f(\mathbf{x}) - f^* \leq \frac{L}{2} d_{\mathcal{X}}(\mathbf{x}, \mathbf{x}^*)^2. \quad (67)$$

The inequality given in Equation A.1.1 in [DX13] states that the geodesic distance on the sphere is bounded by the 2-norm, more precisely, for all  $\mathbf{q}, \mathbf{q}' \in \mathbb{S}^{d-1}$  we have:

$$d_{\mathbb{S}^{d-1}}(\mathbf{q}, \mathbf{q}') \leq \frac{\pi}{2} \|\mathbf{q} - \mathbf{q}'\|. \quad (68)$$

Using  $\mathbf{x} \equiv [\mathbf{q}_1^\top, \dots, \mathbf{q}_n^\top, \mathbf{t}_1^\top, \dots, \mathbf{t}_n^\top]^\top$  and  $\mathbf{x}^* \equiv [(\mathbf{q}_1^*)^\top, \dots, (\mathbf{q}_n^*)^\top, (\mathbf{t}_1^*)^\top, \dots, (\mathbf{t}_n^*)^\top]^\top$  yields:

$$f(\mathbf{x}) - f^* \leq \frac{L}{2} \left( \sum_{i=1}^n d_{\mathbb{S}^3}(\mathbf{q}_i, \mathbf{q}_i^*)^2 + \sum_{i=1}^n \|\mathbf{t}_i - \mathbf{t}_i^*\|^2 \right) \quad (69)$$

$$\leq \frac{L}{2} \left( \frac{\pi^2}{4} \sum_{i=1}^n \|\mathbf{q}_i - \mathbf{q}_i^*\|^2 + \sum_{i=1}^n \|\mathbf{t}_i - \mathbf{t}_i^*\|^2 \right) \quad (70)$$

$$\leq \frac{L\pi^2}{8} \left( \sum_{i=1}^n \|\mathbf{q}_i - \mathbf{q}_i^*\|^2 + \sum_{i=1}^n \|\mathbf{t}_i - \mathbf{t}_i^*\|^2 \right) \quad (71)$$

$$= \frac{L\pi^2}{8} \|\mathbf{x} - \mathbf{x}^*\|^2. \quad (72)$$

This concludes the proof.  $\square$

## I Gradients of Likelihood and Prior Terms

In this section we provide derivations of the gradients for data and prior terms. For completeness, we find it worthy to once again repeat our MAP formulation:

$$\arg \max_{\mathbf{Q}, \mathbf{T}} \left( \sum_{(i,j) \in E} \{ \log p(\mathbf{q}_{ij} | \mathbf{Q}, \mathbf{T}) + \log p(\mathbf{t}_{ij} | \mathbf{Q}, \mathbf{T}) \} + \sum_i \log p(\mathbf{q}_i) + \sum_i \log p(\mathbf{t}_i) \right). \quad (73)$$

We begin by deriving the gradients of the **rotational components** first, and translations second. In the setting where  $\mathbf{V}$  is constant w.r.t.  $\mathbf{q}$  the gradient of log Bingham distribution w.r.t. the random variable  $\mathbf{q}$  reads:

$$\nabla_{\mathbf{x}} \log \mathcal{B}(\mathbf{x}; \Lambda, \mathbf{V}) = \nabla_{\mathbf{x}} \log \frac{1}{F} + \nabla_{\mathbf{x}} (\mathbf{x}^T \mathbf{V} \Lambda \mathbf{V}^T \mathbf{x}) = (\mathbf{V} \Lambda \mathbf{V}^T + \mathbf{V} \Lambda^T \mathbf{V}^T) \mathbf{x} = 2\mathbf{V} \Lambda \mathbf{V}^T \mathbf{x}. \quad (74)$$

Normalizing constant drops as it depends on  $\Lambda$  only [KW07]. We also have cases where  $\mathbf{V}$  is a function of the mode  $\mathbf{q}$ ,  $\mathbf{V} \rightarrow \mathbf{V}(\mathbf{q})$ . Then:

$$\nabla_{\mathbf{q}} \log \mathcal{B}(\mathbf{x}; \Lambda, \mathbf{V}(\mathbf{q})) = \nabla_{\mathbf{q}} (\mathbf{x}^T \mathbf{V}(\mathbf{q}) \Lambda \mathbf{V}^T(\mathbf{q}) \mathbf{x}) = \nabla_{\mathbf{k}} (\mathbf{k}^T \Lambda \mathbf{k}) \nabla_{\mathbf{q}}(\mathbf{k}) = 2\mathbf{k}^T \Lambda \nabla_{\mathbf{q}}(\mathbf{k}), \quad (75)$$

where  $\mathbf{k} = \mathbf{V}^T(\mathbf{q}) \mathbf{x} \in \mathbb{R}^3$  is used to ease the computations. Note that in our particular application it is the case that  $\mathbf{x} \leftarrow \mathbf{q}_{ij}$ , i.e. the data is specified by the relative poses attached to the edges of the graph. We then speak of the gradient of  $\log(p(\mathbf{q}_{ij} | \mathbf{q}_i, \mathbf{q}_j))$  with  $\mathbf{V} \rightarrow \mathbf{V}(\mathbf{q}_j \bar{\mathbf{q}}_i)$  w.r.t.  $\mathbf{q}_i$ . We shorten  $\mathbf{r} \leftarrow \mathbf{q}_j \bar{\mathbf{q}}_i$  and write  $\mathbf{V}$  as a function of  $\mathbf{r}$ ,  $\mathbf{V}(\mathbf{r}) \triangleq \mathbf{V}(\mathbf{q}_j \bar{\mathbf{q}}_i)$ . Then:

$$\nabla_{\mathbf{q}_i} \log \mathcal{B}(\mathbf{x}; \Lambda, \mathbf{V}(\mathbf{r})) = \nabla_{\mathbf{r}} \log \mathcal{B}(\mathbf{x}; \Lambda, \mathbf{V}(\mathbf{r})) \nabla_{\mathbf{q}_i}(\mathbf{r}) = 2\mathbf{k}^T \Lambda \nabla_{\mathbf{r}}(\mathbf{k}) \nabla_{\mathbf{q}_i}(\mathbf{r}), \quad (76)$$

this time with  $\mathbf{k} = \mathbf{V}^T(\mathbf{r}) \mathbf{x} \in \mathbb{R}^3$ . Note that  $\nabla_{\mathbf{r}} \log \mathcal{B}(\mathbf{x}; \Lambda, \mathbf{V}(\mathbf{r}))$  is expanded as in Eq. 75. Using the definition of  $\mathbf{V}$  in Eq. 6, the terms simplify to:

$$\mathbf{k} = \begin{bmatrix} q_1 x_1 + q_2 x_2 + q_3 x_3 + q_4 x_4 \\ q_1 x_2 - q_2 x_1 + q_3 x_4 - q_4 x_3 \\ q_1 x_3 - q_3 x_1 - q_2 x_4 + q_4 x_2 \\ q_1 x_4 + q_2 x_3 - q_3 x_2 - q_4 x_1 \end{bmatrix} \quad \nabla_{\mathbf{q}}(\mathbf{k}) = \begin{bmatrix} x_2 & -x_1 & x_4 & -x_3 \\ x_3 & -x_4 & -x_1 & x_2 \\ x_4 & x_3 & -x_2 & -x_1 \end{bmatrix}. \quad (77)$$

The last term in eq. 76 expands as:

$$\nabla_{\mathbf{q}_i}(\mathbf{q}_j \bar{\mathbf{q}}_i) = \begin{bmatrix} q_{j,1} & q_{j,2} & q_{j,3} & q_{j,4} \\ q_{j,2} & -q_{j,1} & q_{j,4} & -q_{j,3} \\ q_{j,3} & -q_{j,4} & -q_{j,1} & q_{j,2} \\ q_{j,4} & q_{j,3} & -q_{j,2} & -q_{j,1} \end{bmatrix}. \quad (78)$$

We will now derive the gradients for **translational components**. Similarly, we start by the gradient of the log likelihood w.r.t. the data. While a shorter derivation through matrix calculus is also possible, we deliberately provide a longer version, as it might be more intuitive:

$$\begin{aligned} \nabla_{\mathbf{t}} \log \mathcal{N}(\mathbf{t}; \mu, \sigma^2 I) &= \nabla_{\mathbf{t}} \log \frac{1}{G} + \nabla_{\mathbf{t}} \left( -\frac{1}{2} (\mathbf{t} - \mu)^T \Sigma^{-1} (\mathbf{t} - \mu) \right) \\ &= \nabla_{\mathbf{t}} \left( -\frac{1}{2} (\mathbf{t}^T \Sigma^{-1} \mathbf{t} - \mathbf{t}^T \Sigma^{-1} \mu - \mu^T \Sigma^{-1} \mathbf{t} + \mu^T \Sigma^{-1} \mu) \right) \\ &= -\frac{1}{2} (\mathbf{t}^T (\Sigma^{-1} + \Sigma^{-T}) - (\Sigma^{-1} \mu)^T - (\mu^T \Sigma^{-1}) + 0) \\ &= -\frac{1}{2} (2\mathbf{t}^T \Sigma^{-1} - 2\mu^T \Sigma^{-1}) = (\mu^T - \mathbf{t}^T) \Sigma^{-1} \end{aligned} \quad (79)$$

The normalizing constant drops similarly as it does not depend on  $\mathbf{t}$ .

Similar to rotational counterpart, our algorithm centers the data on the mean of the distribution, also requiring to compute the gradients w.r.t. the mean of the distribution. With a derivation similar to but simpler from Eq. 79, it follows:

$$\nabla_{\mu} \log \mathcal{N}(\mathbf{x}; \mu, \sigma^2 I) = -\frac{1}{2} (2\mu^T \Sigma^{-1} - 2\mathbf{x}^T \Sigma^{-1}) = (\mathbf{x}^T - \mu^T) \Sigma^{-1} \quad (80)$$

When we center the distribution on the data, substituting  $\mu \leftarrow \mathbf{t}_j - \mathbf{r} \mathbf{t}_i \bar{\mathbf{r}}$ , where  $\mathbf{r} \leftarrow \mathbf{q}_j \bar{\mathbf{q}}_i$ ,  $\mathbf{x} \leftarrow \mathbf{t}_{ij}$ , we arrive at:

$$\nabla_{\mathbf{t}_i} \log \mathcal{N}(\mathbf{x}; \mu, \sigma^2 I) = \nabla_{\mu} \log \mathcal{N}(\mathbf{x}; \mu, \sigma^2 I) J_{\mathbf{t}_i}(\mu) \quad (81)$$

Note that the first term of the right hand side is given in Eq. 80. The second one can be computed from the derivative of the sandwich action on the 1-blade  $\mathbf{t}_i$ . With slight abuse of notation, in the following we assume that translation-quaternion is purified:  $\mathbf{t}_i \leftarrow [0; \mathbf{t}_i]$ .

$$J_{\mathbf{t}_i}(\mu) = J_{\mathbf{t}_i}(\mathbf{t}_j - \mathbf{r} \mathbf{t}_i \bar{\mathbf{r}}) \quad (82)$$

$$= -J_{\mathbf{t}_i} \left( Q(\bar{\mathbf{r}}) Q(\mathbf{t}_i) \mathbf{r}^T \right) \quad (83)$$

$$= -J_{\mathbf{t}_i} \left( (\mathbf{q}_{ij} \otimes Q(\bar{\mathbf{r}})) \text{vec}(Q(\mathbf{t}_i)) \right) \quad (84)$$

$$= -J_{\mathbf{t}_i} \left( \mathbf{K} \text{vec}(Q(\mathbf{t}_i)) \right) \quad (85)$$

$$= -\mathbf{K} \nabla_{\mathbf{t}_i} \text{vec}(Q(\mathbf{t}_i)) \quad (86)$$

$$= -\mathbf{K} \mathbf{J}_{\mathbf{t}_i} \quad (87)$$

$$= \begin{bmatrix} 0 & 0 & 0 \\ -q_1^2 - q_2^2 + q_3^2 + q_4^2 & 2q_1 q_4 - 2q_2 q_3 & -2q_1 q_3 - 2q_2 q_4 \\ -2q_1 q_4 - 2q_2 q_3 & -q_1^2 + q_2^2 - q_3^2 + q_4^2 & 2q_1 q_2 - 2q_3 q_4 \\ 2q_1 q_3 - 2q_2 q_4 & -2q_1 q_2 - 2q_3 q_4 & -q_1^2 + q_2^2 + q_3^2 - q_4^2 \end{bmatrix} \quad (88)$$

where  $\mathbf{K} \in R^{4 \times 16}$  refers to the Kronecker product matrix  $\mathbf{K} = \mathbf{r} \otimes Q(\bar{\mathbf{q}}_{ij})$ ,  $\mathbf{J}_{\mathbf{t}_i} = \nabla_{\mathbf{t}_i} \text{vec}(Q(\mathbf{t}_i))$  is the  $16 \times 3$  Jacobian matrix and  $\text{vec}(\cdot)$  denotes the linearization operator. Individual components  $q_i$  belong to  $\mathbf{r} = [q_1, q_2, q_3, q_4]$ . The map  $Q(\cdot) : \mathbb{H}_1 \rightarrow R^{4 \times 4}$  constructs a Quaternion matrix form:

$$Q(\mathbf{q}) = \begin{bmatrix} q_1 & -q_2 & -q_3 & -q_4 \\ q_2 & q_1 & q_4 & -q_3 \\ q_3 & -q_4 & q_1 & q_2 \\ q_4 & q_3 & -q_2 & q_1 \end{bmatrix} \quad (89)$$

leading to a more compact notation of the quaternion product. In fact this is not very different from the definition of  $\mathbf{V}(\mathbf{q})$ , as one is free to pick any of the 48 distinct representations out of the matrix ring  $\mathbb{M}(4, \mathbb{R})$ . Note that Eq. 88 has zeros in the initial row. This is due to the property that all the operations respect the purity of the blade. The final Jacobian matrix can be extracted from the remaining three rows corresponding to the vector part.

## J Used Datasets

In order to have a better idea of the nature of the datasets we utilized, it is worthwhile to visualize the camera locations as well as the 3D reconstruction following a full bundle adjustment, that optimizes both 3D points (structure) and 3D poses (motion). In Figure 11, we report 6 such visualizations on 3 outdoor, large scenes, as well as 3 object-scanning scenarios. These plots are not the outcome of our approach, but meant as a reference for the datasets we deal with.

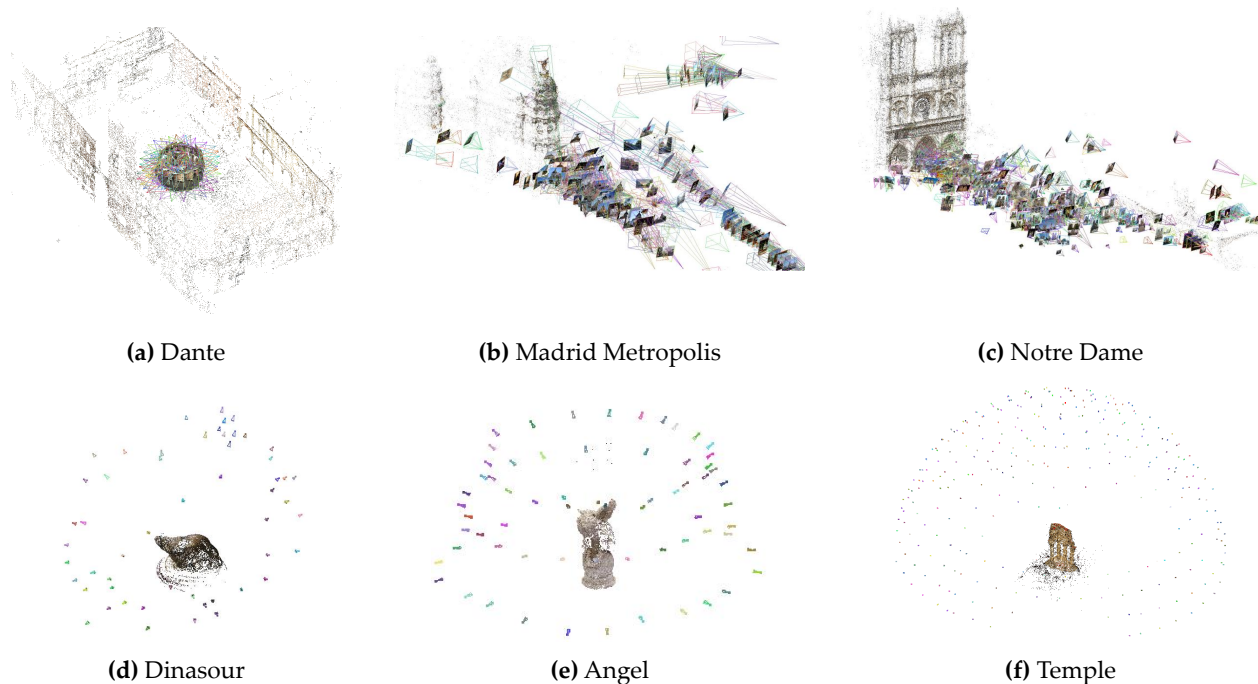


Figure 11: Results of the full bundle adjustment (structure + camera poses) on several datasets.